High-p_T π^0 production with respect to the reaction plane in Au + Au collisions at $\sqrt{s_{NN}} = 200$ GeV

S. Afanasiev,[17] C. Aidala,[7] N. N. Ajitanand,[43] Y. Akiba,[37,38] J. Alexander,[43] A. Al-Jamel,[33] K. Aoki,[23,37] L. Aphecetche,[45] R. Armendariz,[33] S. H. Aronson,[3] R. Averbeck,[44] T. C. Awes,[34] B. Azmoun,[3] V. Babintsev,[14] A. Baldisseri,[8] K. N. Barish,[4] P. D. Barnes,[26] B. Bassalleck,[32] S. Bathe,[4] S. Batsouli,[7] V. Baublis,[36] F. Bauer,[4] A. Bazilevsky,[3] S. Belikov,[3,16,*] R. Bennett,[44] Y. Berdnikov,[40] M. T. Bjorndal,[7] J. G. Boissevain,[26] H. Borel,[8] K. Boyle,[44] M. L. Brooks,[26] D. S. Brown,[33] D. Bucher,[29] H. Buesching,[3] V. Bumazhnov,[14] G. Bunce,[3,38] J. M. Burward-Hoy,[26] S. Butsyk,[44] S. Campbell,[44] J.-S. Chai,[18] S. Chernichenko,[14] J. Chiba,[19] C. Y. Chi,[7] M. Chiu,[7] I. J. Choi,[52] T. Chujo,[49] V. Cianciolo,[34] C. R. Cleven,[12] Y. Cobigo,[8] B. A. Cole,[7] M. P. Comets,[35] P. Constantin,[16] M. Csanád,[10] T. Csörgő,[20] T. Dahms,[44] K. Das,[11] G. David,[3] H. Delagrange,[45] A. Denisov,[14] D. d'Enterria,[7] A. Deshpande,[38,44] E. J. Desmond,[3] O. Dietzsch,[41] A. Dion,[44] J. L. Drachenberg,[1] O. Drapier,[24] A. Drees,[44] A. K. Dubey,[51] A. Durum,[14] V. Dzhordzhadze,[46] Y. V. Efremenko,[34] J. Egdemir,[44] A. Enokizono,[13] H. En'yo,[37,38] B. Espagnon,[35] S. Esumi,[48] D. E. Fields,[32,38] F. Fleuret,[24] S. L. Fokin,[22] B. Forestier,[27] Z. Fraenkel,[51,*] J. E. Frantz,[7] A. Franz,[3] A. D. Frawley,[11] Y. Fukao,[23,37] S.-Y. Fung,[4] S. Gadrat,[27] F. Gastineau,[45] M. Germain,[45] A. Glenn,[46] M. Gonin,[24] J. Gosset,[8] Y. Goto,[37,38] R. Granier de Cassagnac,[24] N. Grau,[16] S. V. Greene,[49] M. Grosse Perdekamp,[15,38] T. Gunji,[5] H. Å. Gustafsson,[28] T. Hachiya,[13,37] A. Hadj Henni,[45] J. S. Haggerty,[3] M. N. Hagiwara,[1] H. Hamagaki,[5] H. Harada,[13] E. P. Hartouni,[25] K. Haruna,[13] M. Harvey,[3] E. Haslum,[28] K. Hasuko,[37] R. Hayano,[5] M. Heffner,[25] T. K. Hemmick,[44] J. M. Heuser,[37] X. He,[12] H. Hiejima,[15] J. C. Hill,[16] R. Hobbs,[32] M. Holmes,[49] W. Holzmann,[43] K. Homma,[13] B. Hong,[21] T. Horaguchi,[37,47] M. G. Hur,[18] T. Ichihara,[37,38] K. Imai,[23,37] M. Inaba,[48] D. Isenhower,[1] L. Isenhower,[1] M. Ishihara,[37] T. Isobe,[5] M. Issah,[43] A. Isupov,[17] B. V. Jacak,[44,†] J. Jia,[7] J. Jin,[7] O. Jinnouchi,[38] B. M. Johnson,[3] K. S. Joo,[30] D. Jouan,[35] F. Kajihara,[5,37] S. Kametani,[5,50] N. Kamihara,[37,47] M. Kaneta,[38] J. H. Kang,[52] T. Kawagishi,[48] A. V. Kazantsev,[22] S. Kelly,[6] A. Khanzadeev,[36] D. J. Kim,[52] E. Kim,[42] Y.-S. Kim,[18] E. Kinney,[6] Á. Kiss,[10] E. Kistenev,[3] A. Kiyomichi,[37] C. Klein-Boesing,[29] L. Kochenda,[36] V. Kochetkov,[14] B. Komkov,[36] M. Konno,[48] D. Kotchetkov,[4] A. Kozlov,[51] P. J. Kroon,[3] G. J. Kunde,[26] N. Kurihara,[5] K. Kurita,[37,39] M. J. Kweon,[21] Y. Kwon,[52] G. S. Kyle,[33] R. Lacey,[43] J. G. Lajoie,[16] A. Lebedev,[16] Y. Le Bornec,[35] S. Leckey,[44] D. M. Lee,[26] M. K. Lee,[52] M. J. Leitch,[26] M. A. L. Leite,[41] H. Lim,[42] A. Litvinenko,[17] M. X. Liu,[26] X. H. Li,[4] C. F. Maguire,[49] Y. I. Makdisi,[3] A. Malakhov,[17] M. D. Malik,[32] V. I. Manko,[22] H. Masui,[48] F. Matathias,[44] M. C. McCain,[15] P. L. McGaughey,[26] Y. Miake,[48] T. E. Miller,[49] A. Milov,[44] S. Mioduszewski,[3] G. C. Mishra,[12] J. T. Mitchell,[3] D. P. Morrison,[3] J. M. Moss,[26] T. V. Moukhanova,[22] D. Mukhopadhyay,[49] J. Murata,[37,39] S. Nagamiya,[19] Y. Nagata,[48] J. L. Nagle,[6] M. Naglis,[51] T. Nakamura,[13] J. Newby,[25] M. Nguyen,[44] B. E. Norman,[26] A. S. Nyanin,[22] J. Nystrand,[28] E. O'Brien,[3] C. A. Ogilvie,[16] H. Ohnishi,[37] I. D. Ojha,[49] H. Okada,[23,37] K. Okada,[38] O. O. Omiwade,[1] A. Oskarsson,[28] I. Otterlund,[28] K. Ozawa,[5] D. Pal,[49] A. P. T. Palounek,[26] V. Pantuev,[44] V. Papavassiliou,[33] J. Park,[42] W. J. Park,[21] S. F. Pate,[33] H. Pei,[16] J.-C. Peng,[15] H. Pereira,[8] V. Peresedov,[17] D. Yu. Peressounko,[22] C. Pinkenburg,[3] R. P. Pisani,[3] M. L. Purschke,[3] A. K. Purwar,[44] H. Qu,[12] J. Rak,[16] I. Ravinovich,[51] K. F. Read,[34,46] M. Reuter,[44] K. Reygers,[29] V. Riabov,[36] Y. Riabov,[36] G. Roche,[27] A. Romana,[24,*] M. Rosati,[16] S. S. E. Rosendahl,[28] P. Rosnet,[27] P. Rukoyatkin,[17] V. L. Rykov,[37] S. S. Ryu,[52] B. Sahlmueller,[29] N. Saito,[23,37,38] T. Sakaguchi,[5,50] S. Sakai,[48] V. Samsonov,[36] H. D. Sato,[23,37] S. Sato,[3,19,48] S. Sawada,[19] V. Semenov,[14] R. Seto,[4] D. Sharma,[51] T. K. Shea,[3] I. Shein,[14] T.-A. Shibata,[37,47] K. Shigaki,[13] M. Shimomura,[48] T. Shohjoh,[48] K. Shoji,[23,37] A. Sickles,[44] C. L. Silva,[41] D. Silvermyr,[34] K. S. Sim,[21] C. P. Singh,[2] V. Singh,[2] S. Skutnik,[16] W. C. Smith,[1] A. Soldatov,[14] R. A. Soltz,[25] W. E. Sondheim,[26] S. P. Sorensen,[46] I. V. Sourikova,[3] F. Staley,[8] P. W. Stankus,[34] E. Stenlund,[28] M. Stepanov,[33] A. Ster,[20] S. P. Stoll,[3] T. Sugitate,[13] C. Suire,[35] J. P. Sullivan,[26] J. Sziklai,[20] T. Tabaru,[38] S. Takagi,[48] E. M. Takagui,[41] A. Taketani,[37,38] K. H. Tanaka,[19] Y. Tanaka,[31] K. Tanida,[37,38] M. J. Tannenbaum,[3] A. Taranenko,[43] P. Tarján,[9] T. L. Thomas,[32] M. Togawa,[23,37] J. Tojo,[37] H. Torii,[37] R. S. Towell,[1] V.-N. Tram,[24] I. Tserruya,[51] Y. Tsuchimoto,[13,37] S. K. Tuli,[2] H. Tydesjö,[28] N. Tyurin,[14] C. Vale,[16] H. Valle,[49] H. W. van Hecke,[26] J. Velkovska,[49] R. Vértesi,[9] A. A. Vinogradov,[22] E. Vznuzdaev,[36] M. Wagner,[23,37] X. R. Wang,[33] Y. Watanabe,[37,38] J. Wessels,[29] S. N. White,[3] N. Willis,[35] D. Winter,[7] C. L. Woody,[3] M. Wysocki,[6] W. Xie,[4,38] A. Yanovich,[14] S. Yokkaichi,[37,38] G. R. Young,[34] I. Younus,[32] I. E. Yushmanov,[22] W. A. Zajc,[7] O. Zaudtke,[29] C. Zhang,[7] J. Zimányi,[20,*] and L. Zolin[17]

(PHENIX Collaboration)

[1]*Abilene Christian University, Abilene, Texas 79699, USA*

[2]*Department of Physics, Banaras Hindu University, Varanasi 221005, India*

[3]*Brookhaven National Laboratory, Upton, New York 11973-5000, USA*

[4]*University of California-Riverside, Riverside, California 92521, USA*

[5]*Center for Nuclear Study, Graduate School of Science, University of Tokyo, 7-3-1 Hongo, Bunkyo, Tokyo 113-0033, Japan*

[6]*University of Colorado, Boulder, Colorado 80309, USA*

[7]*Columbia University, New York, New York 10027 and Nevis Laboratories, Irvington, New York 10533, USA*

[8]*Dapnia, CEA Saclay, F-91191, Gif-sur-Yvette, France*

[9]*Debrecen University, H-4010 Debrecen, Egyetem tér 1, Hungary*

[10]*ELTE, Eötvös Loránd University, H-1117 Budapest, Pázmány P. s. 1/A, Hungary*

[11]*Florida State University, Tallahassee, Florida 32306, USA*

[12]*Georgia State University, Atlanta, Georgia 30303, USA*

[13]*Hiroshima University, Kagamiyama, Higashi-Hiroshima 739-8526, Japan*

[14]*IHEP Protvino, State Research Center of Russian Federation, Institute for High Energy Physics, Protvino, RU-142281, Russia*
[15]*University of Illinois at Urbana-Champaign, Urbana, Illinois 61801, USA*
[16]*Iowa State University, Ames, Iowa 50011, USA*
[17]*Joint Institute for Nuclear Research, RU-141980 Dubna, Moscow Region, Russia*
[18]*KAERI, Cyclotron Application Laboratory, Seoul, Korea*
[19]*KEK, High Energy Accelerator Research Organization, Tsukuba, Ibaraki 305-0801, Japan*
[20]*KFKI Research Institute for Particle and Nuclear Physics of the Hungarian Academy of Sciences (MTA KFKI RMKI), H-1525 Budapest 114, P. O. Box 49, Budapest, Hungary*
[21]*Korea University, Seoul, 136-701, Korea*
[22]*Russian Research Center "Kurchatov Institute," Moscow, Russia*
[23]*Kyoto University, Kyoto 606-8502, Japan*
[24]*Laboratoire Leprince-Ringuet, Ecole Polytechnique, CNRS-IN2P3, Route de Saclay, F-91128, Palaiseau, France*
[25]*Lawrence Livermore National Laboratory, Livermore, California 94550, USA*
[26]*Los Alamos National Laboratory, Los Alamos, New Mexico 87545, USA*
[27]*LPC, Université Blaise Pascal, CNRS-IN2P3, Clermont-Fd, 63177 Aubiere Cedex, France*
[28]*Department of Physics, Lund University, Box 118, SE-221 00 Lund, Sweden*
[29]*Institut für Kernphysik, University of Muenster, D-48149 Muenster, Germany*
[30]*Myongji University, Yongin, Kyonggido 449-728, Korea*
[31]*Nagasaki Institute of Applied Science, Nagasaki-shi, Nagasaki 851-0193, Japan*
[32]*University of New Mexico, Albuquerque, New Mexico 87131, USA*
[33]*New Mexico State University, Las Cruces, New Mexico 88003, USA*
[34]*Oak Ridge National Laboratory, Oak Ridge, Tennessee 37831, USA*
[35]*IPN-Orsay, Universite Paris Sud, CNRS-IN2P3, BP1, F-91406, Orsay, France*
[36]*PNPI, Petersburg Nuclear Physics Institute, Gatchina, Leningrad region, RU-188300, Russia*
[37]*RIKEN Nishina Center for Accelerator-Based Science, Wako, Saitama 351-0198, Japan*
[38]*RIKEN BNL Research Center, Brookhaven National Laboratory, Upton, New York 11973-5000, USA*
[39]*Physics Department, Rikkyo University, 3-34-1 Nishi-Ikebukuro, Toshima, Tokyo 171-8501, Japan*
[40]*Saint Petersburg State Polytechnic University, St. Petersburg, Russia*
[41]*Universidade de São Paulo, Instituto de Física, Caixa Postal 66318, São Paulo CEP05315-970, Brazil*
[42]*System Electronics Laboratory, Seoul National University, Seoul, Korea*
[43]*Chemistry Department, Stony Brook University, Stony Brook, SUNY, New York 11794-3400, USA*
[44]*Department of Physics and Astronomy, Stony Brook University, SUNY, Stony Brook, New York 11794, USA*
[45]*SUBATECH (Ecole des Mines de Nantes, CNRS-IN2P3, Université de Nantes) BP 20722-44307, Nantes, France*
[46]*University of Tennessee, Knoxville, Tennessee 37996, USA*
[47]*Department of Physics, Tokyo Institute of Technology, Oh-okayama, Meguro, Tokyo 152-8551, Japan*
[48]*Institute of Physics, University of Tsukuba, Tsukuba, Ibaraki 305, Japan*
[49]*Vanderbilt University, Nashville, Tennessee 37235, USA*
[50]*Waseda University, Advanced Research Institute for Science and Engineering, 17 Kikui-cho, Shinjuku-ku, Tokyo 162-0044, Japan*
[51]*Weizmann Institute, Rehovot 76100, Israel*
[52]*Yonsei University, IPAP, Seoul 120-749, Korea*
(Received 30 March 2009; published 13 November 2009)

Measurements of the azimuthal anisotropy of high-p_T neutral pion (π^0) production in Au + Au collisions at $\sqrt{s_{NN}} = 200$ GeV by the PHENIX experiment are presented. The data included in this article were collected during the 2004 Relativistic Heavy Ion Collider running period and represent approximately an order of magnitude increase in the number of analyzed events relative to previously published results. Azimuthal angle distributions of π^0 mesons detected in the PHENIX electromagnetic calorimeters are measured relative to the reaction plane determined event-by-event using the forward and backward beam-beam counters. Amplitudes of the second Fourier component (v_2) of the angular distributions are presented as a function of π^0 transverse momentum (p_T) for different bins in collision centrality. Measured reaction plane dependent π^0 yields are used to determine the azimuthal dependence of the π^0 suppression as a function of p_T, $R_{AA}(\Delta\phi, p_T)$. A jet-quenching motivated geometric analysis is presented that attempts to simultaneously describe the centrality dependence and reaction plane angle dependence of the π^0 suppression in terms of the path lengths of hypothetical parent partons in the medium. This set of results allows for a detailed examination of the influence of geometry in the collision region and of the interplay between collective flow and jet-quenching effects along the azimuthal axis.

DOI: 10.1103/PhysRevC.80.054907 PACS number(s): 21.65.Qr, 25.75.Dw

I. INTRODUCTION

Over the past few years, experiments at the Relativistic Heavy Ion Collider (RHIC) have established that a dense partonic medium is formed in Au + Au collisions at $\sqrt{s_{NN}} =$ 200 GeV [1–4]. This medium thermalizes very quickly [1,5–11] and is extremely opaque to the passage of high-p_T particles [12,13], and the strong coupling of matter in the medium produces a system for which the ratio of shear viscosity to entropy (η/s) approaches zero [14–18]. Much of the current focus is on the extraction of key transport and thermodynamic characteristics of the matter produced in these collisions. Measurements of high-p_T parton propagation in the medium as well as medium-induced modification of the fragmentation parton spectrum and its products provide a critical tool for probing medium properties.

One of the most striking early results from RHIC was the observation of strongly suppressed production of high-p_T particles in central Au + Au events compared to appropriately scaled $p + p$ collisions [12,13]. High-p_T partons are formed from hard scattering between the initial colliding partons, and these partons fragment into two or more jets of hadrons. When propagating through a dense volume of deconfined matter, these high-p_T partons are expected to scatter from color charges in the medium, losing energy through a combination of gluon bremsstrahlung radiation and collisional energy transfer to partons in the medium (see e.g. [19]). These radiated gluons eventually fragment into hadrons at lower p_T, resulting in a depletion of the observed yields of hadrons at higher p_T.

A useful way to quantify the suppression of high-p_T hadrons is the nuclear modification factor ($R_{\rm AA}$) where the $p + p$ cross section is scaled by the thickness function $\langle T_{\rm AA}\rangle$ of the two Au nuclei

$$R_{\rm AA}(p_T) = \frac{\left(1/N_{\rm AA}^{\rm evt}\right) d^2N_{\rm AA}^{\pi^0}/dp_T dy}{\langle T_{\rm AA}\rangle \times d^2\sigma_{pp}^{\pi^0}/dp_T dy}.$$

PHENIX has measured a $\pi^0 R_{\rm AA}$ close to unity in both peripheral Au + Au collisions and d + Au collisions [20,21], consistent with the expectation that these collisions would not produce an extended, dense medium. As the collisions become more central, $R_{\rm AA}$ decreases to about 0.2, indicating a stronger parton energy loss. Furthermore, the measured $\pi^0 R_{\rm AA}$ is nearly constant as a function of p_T, for $p_T \gtrsim 5$ GeV/c up to the highest currently accessible p_T, 20 GeV/c [20].

These data can be well reproduced by models that calculate the energy lost by the hard scattered partons as they traverse the dense medium. The amount of energy loss depends on the density of the medium [22], so measurements of high-p_T hadron suppression provide constraints on the transport coefficient $\langle\hat{q}^2\rangle$, a measure of mean transverse momentum squared $\langle k_{\rm T}^2\rangle$ transferred by the medium to a high-energy parton. However, multiple models with different physical assumptions can reproduce the measured $R_{\rm AA}(p_T)$ [23]. The different models vary widely in how they include the crucial interference terms between multiple-scattering centers as well as the interplay among inelastic, elastic, and flavor-changing processes during the parton's passage.

To discriminate between these models we need to increase our experimental control of the path length, because the amount of energy lost by a high-p_T parton strongly increases with the distance traveled through the medium. A quadratic dependence on the path length is predicted for a static medium if the dominant energy-loss mechanism is the bremsstrahlung radiation of gluons surviving the destructive interference caused by multiple scattering [23]. For an expanding plasma the quadratic increase should be moderated to a linear dependence [24].

The centrality dependence of $R_{\rm AA}(p_T)$ offers a probe of the path-length dependence of partonic energy loss. However, we can better test the path-length dependence by studying the azimuthal variation of the high-p_T suppression at a fixed centrality. Because the collision zone has a nearly elliptical shape in the transverse plane due to the noncentral overlap of the colliding Au nuclei, partons that travel along the short axis of the nuclear overlap region lose less energy and should therefore be less suppressed. The key observable is then the two-dimensional modification factor $R_{\rm AA}(\Delta\phi, p_T)$, where $\Delta\phi$ is the angle of emission with respect to the event plane. The azimuthal dependence of the spectra can also be parameterized by a Fourier expansion, where up to second order $\frac{dN}{d\Delta\phi} = N_0[1 + 2v_2\cos(2\Delta\phi)]$, with v_2 being called elliptic flow coefficient. While both quantities characterize azimuthal asymmetries, historically and conceptually they have different roots. The notion of elliptic flow is primarily tied to lower-p_T phenomena ("soft physics"), the domain where particle production is proportional to the number of participating nucleons ($N_{\rm part}$), and positive v_2 arises from the *boost* to the mean p_T in the direction where the pressure gradient is highest (along the reaction plane). Conversely, $R_{\rm AA}(p_T)$ and $R_{\rm AA}(\Delta\phi, p_T)$ are commonly used to describe high-p_T behavior (hard scattering, which scales with the number of binary collisions $N_{\rm coll}$). When $R_{\rm AA}$ deviates from unity at high p_T, it becomes a valuable probe of the *loss* of energy/momentum in a particular direction. However, there is no clear separation between soft and hard regions, and both $R_{\rm AA}$ and v_2 are well defined in the entire momentum range, so in this sense v_2 is sensitive to differential energy loss at high p_T.

PHENIX has measured high-p_T v_2 for π^0 particles from Au + Au collisions [25]. The energy-loss models that reproduce $R_{\rm AA}(p_T)$ diverge in their predictions of the azimuthal anisotropy at high p_T. They generally underpredict the observed azimuthal variation of $R_{\rm AA}(\Delta\phi)$ or, equivalently, are unable to describe the p_T dependence of v_2 over the full range of p_T where one would naively expect them to be applicable [26–28]. These models include the hydrodynamical evolution of the medium, and therefore the high-p_T probe loses energy in a medium that is becoming spatially isotropic with time. Several early articles noticed that the measured v_2 values were larger than what one would expect from a completely opaque almond-shape collision zone [29,30]. Other early energy-loss calculations came close to reproducing the measured $R_{\rm AA}(\Delta\phi)$ [31,32], but in these the plasma expansion was not taken into account, which resulted in unrealistically

*Deceased.
†PHENIX Spokesperson: jacak@skipper.physics.sunysb.edu

strong azimuthal anisotropy. Recent calculations, surveyed in Ref. [27], reproduced the general trend of $R_{\rm AA}(\Delta\phi)$ but not the absolute magnitude and its p_T dependence.

One potential resolution of the problem with energy-loss calculations not reproducing the measured azimuthal dependence of yields is a recent calculation that allowed the high-p_T parton to resonantly scatter with the medium [33], increasing the energy lost by a parton at plasma densities that correspond to temperatures near the critical temperature. This produces a sharper dependence of the energy loss on the spatial variation of the medium's energy density and hence the model is able to simultaneously reproduce both $R_{\rm AA}(p_T)$ and $R_{\rm AA}(\Delta\phi)$. A critical check will be to examine whether the same parameters work for the full range of collision centralities.

To discriminate among all the models that attempt to reproduce $R_{\rm AA}(\Delta\phi, p_T)$, the experimental challenge is to extend the range and increase the precision of observations that can be used to test different energy-loss models. In this article we extend the range of published data on $R_{\rm AA}(\Delta\phi)$ [34] by (a) reaching higher p_T and thereby moving to a p_T region that is completely dominated by the fragmentation of hard partons and reducing the possible contribution of particles from recombination [35]; (b) using finer bins in centrality, thus achieving less averaging of the path length; and (c) reducing the statistical and systematic uncertainties to further constrain models. We present in this article measurements using data collected during the 2004 RHIC running period. These data represent a high-statistics sample of Au + Au collisions (approximately 50 times that of the 2002 RHIC running period) and therefore extend our ability to measure $R_{\rm AA}(\Delta\phi)$ and v_2 to much higher p_T with better precision.

II. EXPERIMENTAL DETAILS

The data presented in this article were taken by the PHENIX experiment [36] in 2004 (RHIC Run-4) and represent the analysis of 821M minimum bias Au + Au collisions at $\sqrt{s_{NN}} = 200$ GeV. The detectors involved in this analysis are the beam-beam counters [37] (BBC, triggering, centrality, and reaction plane determination), the zero-degree calorimeter [38] (ZDC, centrality determination), and the electromagnetic calorimeter [39] (EMCal, π^0 measurement).

The BBCs are two groups of 64 hexagonal quartz Čerenkov radiator counters with photomultiplier readout surrounding the beampipe 144 cm up- and downstream ("north" and "south") from the center of the nominal collision diamond, covering the $3 < |\eta| < 3.9$ pseudorapidity range and the full azimuth. Coincidence of signals in at least two photomultiplier tubes in both BBCs served as a minimum-bias trigger and according to simulations it captured 92% of all inelastic collisions. The size of the total signal in the BBCs increases monotonically with collision centrality at this $\sqrt{s_{NN}}$. The collision vertex z was calculated with $\sigma < 2.0$ cm resolution from the difference between the fastest timing signals in the north and south BBCs, respectively. Only events with $|z| < 30$ cm were analyzed.

The ZDCs are small tungsten/scintillator hadron calorimeters with quartz fiber lightguides and photomultiplier readout, located between the beampipes at 18 m north and south from the collision point. They measure noninteracting "spectator" neutrons in a cone of about 2 mrad, and their signal is double-valued as a function of centrality (it is low in very central and very peripheral collisions but large at midcentrality). The correlation of ZDC vs. BBC signals resolves this ambiguity and allows a precise measurement of the true centrality for all but the most peripheral collisions.

The reaction plane (spanned by the beam direction and the impact vector of the colliding nuclei) is determined event by event from the azimuthal charge distribution in the BBCs, after taking into account small nonuniformities (in the response of individual radiators, PMTs, electronics, etc.), using the assumption that over a large number of events the ϕ distribution of per-event reaction planes should be uniform. Due to the large rapidity gap between the central arm ($|\eta| < 0.35$), where π^0s are measured, and the BBCs, where the reaction plane is established, we assume that the reaction plane is unbiased and free from autocorrelations. However, the relatively coarse granularity of the BBCs affects the resolution. Note that in this analysis precise knowledge of the reaction plane resolution, which depends strongly on centrality, is crucial. This will be discussed in detail in the next section.

Neutral pions are measured by reconstructing their decay photons ($\pi^0 \to \gamma\gamma$) in the EMCal. The EMCal consists of eight sectors at midrapidity ($|\eta| < 0.35$), covering a total of $2 \times 90^\circ$ in azimuth. Six sectors are lead/scintillator (PbSc) sampling calorimeter with photomultiplier readout and 5.5×5.5 cm^2 granularity, and two sectors are lead glass (PbGl) Čerenkov counters with 4×4 cm^2 granularity and photomultiplier readout. The two detectors are $18X_0$ and $16X_0$ radiation lengths deep, respectively, both ensuring essentially full containment of electromagnetic showers in the relevant energy range. The *in situ* energy resolution is well reproduced by simulation both in PbSc and PbGl: the π^0 peak positions and the widths both agree with the data to better than 1 MeV over the entire momentum range. Therefore, the error on the energy (and momentum) scale is less than 1%. Timing resolution σ_t is ~450 ps and ~650 ps for the PbSc and PbGl, respectively. Such good timing resolution allowed the rejection of neutrons and antineutrons up to a few GeV/c transverse momentum, which would otherwise be a major source of neutral showers up to a few GeV energy. At sufficiently high transverse momenta, decay photons from a nearly symmetric ($E_{\gamma_1} \approx E_{\gamma_2}$) decay may produce showers in the calorimeter that start to merge into one reconstructed cluster. In the PbSc this effect is first visible around $p_T \sim 10$ GeV/c, at the upper end of the p_T region considered in this article. Due to its higher granularity and smaller Molière-radius the PbGl is immune to this "merging" problem up to $p_T \sim 15$ GeV/c. The hadronic response, timing properties and other sources of systematic errors are very different for the two calorimeter types. Therefore, when extracting the ϕ-integrated $R_{\rm AA}$, which serves as absolute normalization, the PbSc and PbGl were analyzed separately and the results combined to decrease the total systematic uncertainty.

III. DATA ANALYSIS

A. Centrality

As mentioned, the minimum-bias trigger in the Run-4 PHENIX configuration is supplied by the BBCs, and the correlation of the charge deposited in the BBCs with energy deposited in the ZDCs provides a determination of the centrality of the collision. The v_2 measurement presented in this article is measured in seven bins of the centrality range 0–92%, with the lowest corresponding to the most central: 0–5%, 5–10%, 10–20%, 20–30%, 30–40%, 40–50%, and 50–60%. In addition, the combined ranges 0–20%, 20–40%, 40–60%, and minimum-bias bins are included. For the yields with respect to the reaction plane, the centralities presented are 0–10%, 10–20%, 20–30%, 30–40%, 40–50%, 50–60%. Finally, the $R_{\rm AA}$ versus nuclear path length result excludes the most central bin due to its smaller intrinsic ellipticity (the average path length is insensitive to $\Delta\phi$).

B. Reaction plane determination

The technique used to determine the reaction plane on an event-by-event basis is the same used in previous PHENIX analyses [14,25,40]. The quartz radiators of each counter are arranged in approximately concentric circles around the beam axis. The light collected in the photomultiplier tubes (PMTs) allows for an estimate of the number of charged particles passing through the detector.

The number of charged particles at a given PMT position, N_i, is weighted in a manner to reduce the bias of the inner rings and used to measure the orientation of the reaction plane from the formula

$$\tan(2\Psi) = \frac{\sum_i w_i N_i \sin(2\phi_i) - \langle \sum_i w_i N_i \sin(2\phi_i)\rangle}{\sum_i w_i N_i \cos(2\phi_i) - \langle \sum_i w_i N_i \cos(2\phi_i)\rangle}, \quad (1)$$

where ϕ_i is the nominal azimuth of the radiator. Subtraction of the average centroid removes biases due to various detector effects. A final flattening technique is used to remove the residual nonuniformities in the distribution of angles.

To estimate the resolution of the reaction plane measurement, we use the subevent technique [41]. The approach consists of dividing the event up into two subevents roughly equal in size. The two individual BBCs provide a natural subevent division, so we analyze the distribution of event-by-event differences between the reaction plane angles measured in the north and south counters, $\Delta\Psi = \Psi_N - \Psi_S$. In the presence of pure flow, this distribution takes the form [41]:

$$\frac{dN}{d\Delta\Psi} = \frac{e^{-\chi^2}}{2}\left\{\frac{2}{\pi}(1+\chi^2) + z\,[I_0(z) + \mathrm{L}_0(z)] + \chi^2\,[I_1(z) + \mathrm{L}_1(z)]\right\} \quad (2)$$

where $z = \chi^2 \cos(2\Delta\Psi)$ and the functions I_n and L_n are the modified Bessel functions of the first kind and modified Struve functions, respectively. The parameter χ describes the dispersion of the flow $\vec{Q}$ vector and thus determines the correction required for the reaction plane resolution. Because $\Delta\Psi$ represents the whole-event difference distribution and we are dealing with subevents with roughly half the multiplicity of the event, we replace $\chi \to \chi/\sqrt{2}$ in Eq. (2) and fit this function to the measured $\Delta\Psi$ distribution to extract χ. The resulting value is then used to evaluate the resolution of the event-plane of nth order [41]:

$$\langle \cos n\,(\Psi - \Psi_{\rm RP})\rangle = \frac{\sqrt{\pi}}{2}\chi e^{-\frac{\chi^2}{2}}\left[I_{\frac{n-1}{2}}\left(\frac{\chi^2}{2}\right) + I_{\frac{n+1}{2}}\left(\frac{\chi^2}{2}\right)\right], \quad (3)$$

where the true reaction plane orientation is denoted by $\Psi_{\rm RP}$ and the observed orientation by Ψ. Figure 1 shows the resolution correction obtained using the above-described procedure as a function of centrality. Both 5% and 10% wide bins are shown for comparison.

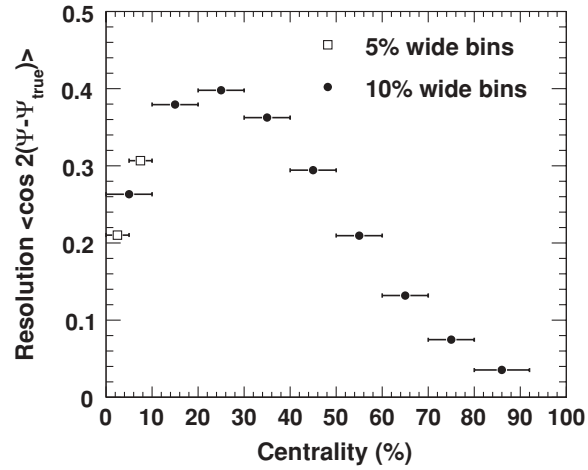

FIG. 1. Reaction plane resolution correction as a function of centrality.

Equation (2) is derived under the assumption that the azimuthal distributions are free of nonflow effects. Due to the large rapidity gap between the BBCs and the central arm region, it is expected that particles observed in the BBCs have no correlation with those measured in the central arm detectors. PYTHIA [42] studies have been used to confirm that jets observed in the central arm have negligible effect on the reaction plane measurement from the BBCs [43].

C. Neutral pion measurement

Measurement of neutral pions has played a critical role in the study of high-p_T phenomena at RHIC and especially by PHENIX [12,20,34]. The two-particle decay channel $\pi^0 \to \gamma + \gamma$ provides a clean signal of identified hadrons out to the highest-p_T regions.

EMCal showers are found by clustering contiguous towers with energy above a threshold energy (10 MeV) and requiring at least 50 MeV in the tower with highest energy deposit. The impact position is calculated from the positions of the participating towers weighted by the logarithm of deposited energy. The energy of the cluster is corrected for nonperpendicular incidence—the angle being derived by assuming a straight path between the actual vertex and the calculated impact point—as well as nonlinearities [34]. In

high-multiplicity events such as central Au + Au collisions, there is an increasing probability for clusters to overlap (one tower accumulates energy from more than one particle), which can distort an energy measurement from a simple sum over contiguous towers. To mitigate this effect, the EMCal clustering algorithm also provides a quantity called *ecore*, which is determined by extrapolating the "core" energy represented by the central four or five towers in the cluster, assuming an electromagnetic shower profile. The energy- and impact angle-dependent shower profile is a model developed from and checked against beam test data. In this way, *ecore* provides a more realistic measurement of the shower energy that is less prone to contributions from accidental overlaps (particles hitting close enough to deposit energy in the same towers) than a simple energy sum of participating towers would be. We use this *ecore* for the energy of reconstructed clusters in this analysis.

The invariant mass of a photon pair γ_i, γ_j as measured in the EMCal is calculated from the energy of the clusters and their measured position:

$$m_{\gamma_i\gamma_j} = \sqrt{\left(P_{\gamma_i}^2 + P_{\gamma_j}^2\right)} = \sqrt{2E_iE_j\cos(1-\theta_{ij})}, \qquad (4)$$

where θ_{ij} is the opening angle between the two photons and $m_{\gamma_i\gamma_j}$ is equal to the π^0 mass for photons from the decay of the same π^0. Because the photons from the π^0 are not tagged, such pairs have to be formed from each photon pair in the event where the pair momentum falls in a particular p_T bin, and some of these pairs might accidentally reproduce the π^0 mass as well (combinatorial background), particularly at lower p_T and higher centralities (multiplicities). Because π^0s cannot be uniquely identified, raw π^0 yields are extracted statistically, by subtracting the combinatorial background from the invariant mass distribution.

A well-known technique to reduce the combinatorial background is to place a cut on the energy asymmetry of the pair, as defined by:

$$\alpha = \frac{|E_1 - E_2|}{E_1 + E_2} = \beta|\cos\theta^*|. \qquad (5)$$

Because the angular distribution $d\sigma/d\cos\theta^*$ of the pairs in the rest frame of the π^0 is uniform, the asymmetry distribution should be flat. However, due to the steeply falling photon spectrum, fake (noncorrelated) pairs that still give the proper π^0 mass are strongly peaked toward $\alpha = 1$. A pair of clusters in the EMCal is considered a neutral pion candidate only if the pair's asymmetry is less than 0.8. In addition, the two photons are required to be separated by at least 8 cm for the combination to be considered as a π^0 candidate.

There remains a nontrivial background contribution that passes these cuts: pairs of photons from different π^0s or, more generally, from pairs of uncorrelated clusters that pass the photon identification cuts and accidentally give an invariant mass near the true π^0 mass. This remaining combinatorial background is estimated and subtracted using the event mixing method. The procedure involves forming pairs from different events, which will by definition be uncorrelated. Each photon candidate is combined with all the photon candidates in previous events stored in memory. To replicate the background from uncorrelated pairs within the same event as closely as possible in the mixed events, mixing is performed within bins of centrality, vertex z position, and reaction plane orientation. Because all events analyzed are minimum bias, no special steps are needed to avoid the distortions of the mixed-event background by the trigger requirement. All cuts applied to the combinations of same event pairs are also applied to mixed-event pairs. The number of events buffered determines the statistics of the mixed-event distributions, chosen as a trade-off between desired statistical accuracy and computational resources. The data presented in this article are mixed with five previous events (in each centrality, vertex, and reaction plane bin).

For a given p_T bin, the mixed-event mass distribution is normalized to the same-event distribution in a region away from the π^0 mass peak. The normalization region is 0.25–0.45 GeV/c^2 for $p_T < 6.0$ GeV/c and 0.21–0.45 GeV/c^2 otherwise. Figure 2 shows an example of this subtraction process at moderate p_T for two centrality bins.

The scaled background distribution is then subtracted from the same-event pair distribution. The subtracted result thus represents a sample of real π^0s. The peak is fit to a Gaussian to determine its width and mean position. The raw yield of π^0s is determined by integrating the counts in a window of $\pm 2\sigma$ around the mean. The width and mean are recorded and parameterized as a function of p_T and centrality based on this ϕ-integrated, large sample. The positions and widths from this parametrization are then used when we extract the (much smaller) raw yields in bins of angle $\Delta\phi$ with respect to the reaction plane. The maximum variation of the yields (multiplicities) with $\Delta\phi$ is only about a factor of 2, and therefore the means and widths are not expected to change substantially. Furthermore, the statistics are much poorer in the $\Delta\phi$ bins, which would make individual π^0 fits unreliable.

There is a residual background in the invariant mass distributions even after the mixed-event distribution has been removed, especially at lower p_T (below ~2 GeV/c). This is due to correlations that event mixing cannot reproduce, like the "subevent structure" due to the presence of jets or multiple, close-by showers from an annihilating anti-neutron, or imperfections of the reconstruction algorithm, such as cluster merging, cluster splitting, and other contributions. Much of the residual background is excluded by starting the fit at 0.09 GeV/c. What is left is accounted for by including a first-order polynomial in the fits to the (already background-subtracted) invariant mass distribution and subtracting its integral from the raw π^0 yield (see Fig. 2). In the more central events, the peak deviates slightly from Gaussian on the high-mass side, due to overlapping clusters. The use of *ecore* mitigates this effect, and the systematic uncertainty on yield extraction arising from the remaining asymmetry has been estimated to be 3–4% [20].

D. Elliptic flow measurement

To obtain the azimuthal angle dependence of π^0 production, we measure raw π^0 yields in a given p_T bin as a function of the π^0 angle with respect to the reaction plane orientation

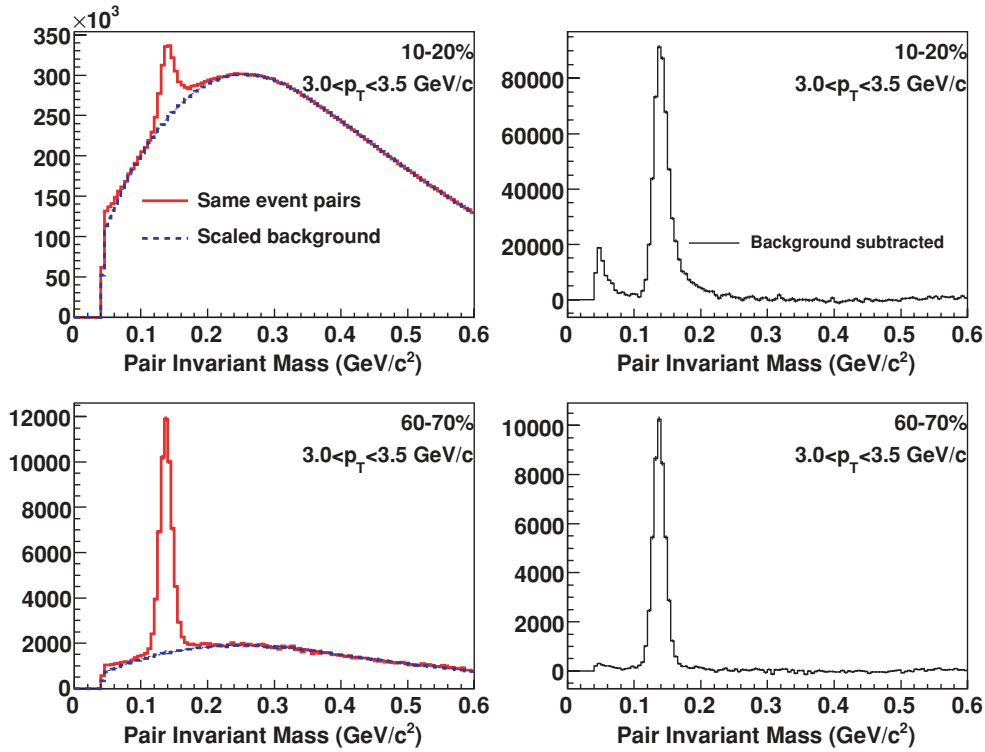

FIG. 2. (Color online) Invariant mass distributions at moderate p_T and two different centralities. (Left panels) Same event and normalized mixed-event distributions. (Right panel) The subtracted distributions, which are then fit with the sum of a first degree polynomial and a Gaussian.

in six equally spaced bins of $\Delta\phi = \phi(\pi^0) - \Psi_{\rm RP}$ covering the range $0 < \Delta\phi < \pi/2$. The π^0 yields are measured in each $\Delta\phi$ bin using the same procedure described in Sec. III C for the reaction-plane inclusive measurement except that the mass fits are not performed in each $\Delta\phi$ bin. Instead, the peak integration window is set $\pm 2\sigma$ around the mean where the width and mean are taken from the inclusive analysis. The resulting raw π^0 angular distribution $dN/d\Delta\phi$ can then be fit to determine the strength of the modulation in the yield. Because the PHENIX BBCs have uniform azimuthal coverage, the π^0 measurements have uniform acceptance in $\Delta\phi$ when averaged over a large event sample, despite the limited azimuthal acceptance of the PHENIX electromagnetic calorimeters.

Assuming elliptic flow is the dominant source of $\Delta\phi$ variation in the π^0 yields, we perform a fit to the angular distributions of the form

$$\frac{dN}{d\Delta\phi} = N_0\left(1 + 2v_2^{\rm meas}\cos 2\Delta\phi\right). \tag{6}$$

We use an analytic linear χ^2 fitting procedure that matches the integral of Eq. (6) over each of the $\Delta\phi$ bins to the measured π^0 yield within the corresponding bin. In the definition of the χ^2 function we account for nonzero covariances between the yields in the different $\Delta\phi$ bins resulting from the limited acceptance of the calorimeters. These covariances have been evaluated separately for each p_T and centrality bin. Examples of the raw $dN/d\Delta\phi$ distributions and the results of the χ^2 fits are shown in Fig. 3. The resulting $v_2^{\rm meas}$ values are then corrected upward to account for reaction plane resolution using correction factors described in Sec. III B.

E. $R_{\rm AA}(\Delta\phi)$ measurement

The nuclear modification factor $R_{\rm AA}$ has played a critical role in understanding energy-loss mechanisms. $R_{\rm AA}$ is defined as

$$R_{\rm AA}(p_T) = \frac{\left(1/N_{\rm AA}^{\rm evt}\right)d^2N_{\rm AA}^{\pi^0}/dp_Tdy}{\langle T_{\rm AA}\rangle \times d^2\sigma_{pp}^{\pi^0}/dp_Tdy}, \tag{7}$$

where $\langle T_{\rm AA}\rangle$ is the mean Glauber overlap function for the centrality being analyzed:

$$\langle T_{\rm AA}\rangle \equiv \frac{\int T_{\rm AA}(\mathbf{b})d\mathbf{b}}{\int\left(1 - e^{-\sigma_{pp}^{\rm inel}T_{\rm AA}(\mathbf{b})}\right)d\mathbf{b}}, \tag{8}$$

from which the mean number of binary nucleon-nucleon collisions can be calculated, $\langle N_{\rm coll}\rangle = \sigma_{pp}^{\rm inel}\langle T_{\rm AA}\rangle$.

For each p_T bin, we can calculate the ratio

$$R(\Delta\phi_i, p_T) = \frac{N(\Delta\phi_i, p_T)}{\sum_{i=1}^{6} N(\Delta\phi_i, p_T)}, \tag{9}$$

where $N(\Delta\phi_i, p_T)$ is the number of π^0s observed in the given $(\Delta\phi_i, p_T)$ bin. Because the BBC is azimuthally symmetric the PHENIX acceptance has no $\Delta\phi$ dependence, and there should be no azimuthal dependence to efficiency and acceptance corrections. As a result,

$$R_{\rm AA}(\Delta\phi_i, p_T) = R(\Delta\phi_i, p_T) \times R_{\rm AA}(p_T). \tag{10}$$

Thus, we can use measured inclusive $R_{\rm AA}(p_T)$ to convert $R(\Delta\phi_i, p_T)$ to $R_{\rm AA}(\Delta\phi_i, p_T)$. Because the detector efficiency and acceptance corrections are already contained in $R_{\rm AA}(p_T)$, there is no need to apply them to $R(\Delta\phi_i, p_T)$.

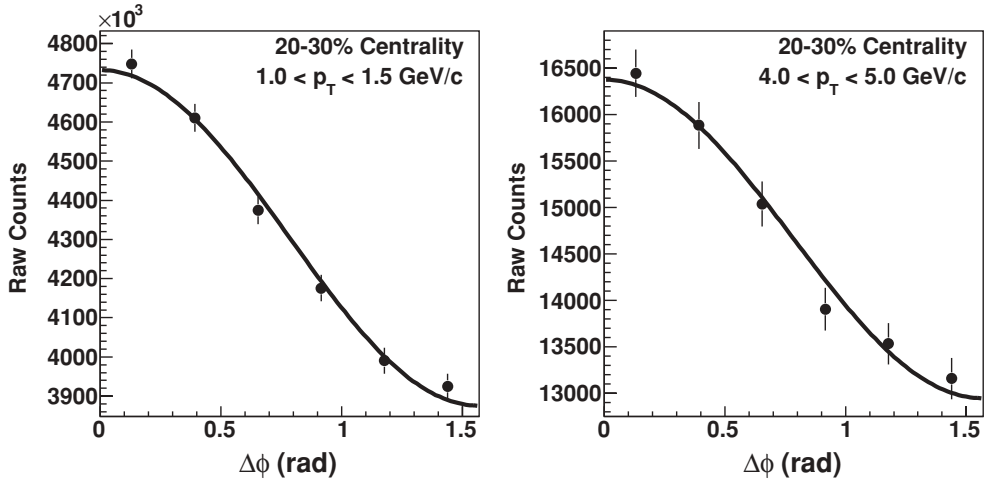

FIG. 3. Example of analytic fitting of raw $dN/d\Delta\phi$ distributions.

Prior to calculating $R_{\rm AA}(\Delta\phi_i, p_T)$ we correct the ratios $R(\Delta\phi_i, p_T)$ for the finite reaction plane resolution using an approximate unfolding technique. For a pure flow $\Delta\phi$ distribution, we can express the influence of the resolution broadening on the measured $\Delta\phi$ distribution

$$R^{\rm meas}(\Delta\phi_i, p_T) = R^{\rm true}(\Delta\phi_i, p_T)\left[\frac{1+2v_2^{\rm meas}\cos(2\Delta\phi)}{1+2v_2^{\rm cor}\cos(2\Delta\phi)}\right], \tag{11}$$

where according to the results of Sec. III B $v_2^{\rm meas} = v_2^{\rm cor}/\langle\cos 2(\Psi - \Psi_{\rm RP})\rangle$. Then, if the measured $\Delta\phi$ distribution resulted from pure elliptic flow, it could be corrected back to the true distribution by

$$R^{\rm cor}(\Delta\phi_i, p_T) = R^{\rm meas}(\Delta\phi_i, p_T)\left[\frac{1+2v_2^{\rm cor}\cos(2\Delta\phi)}{1+2v_2^{\rm meas}\cos(2\Delta\phi)}\right]. \tag{12}$$

As shown above, the general features of the measured $\pi^0\Delta\phi$ distributions are well described by pure $\cos(2\Delta\phi)$ modulation. However, we wish to preserve in our measurements of the azimuthal dependence of the π^0 production the full shape of the measured $\Delta\phi$ distribution, including possible small nonelliptic contributions. For this purpose, the correction described in Eq. (12) applied to the data represents an approximation to a full unfolding procedure that becomes exact when the distribution is purely $\cos(2\Delta\phi)$ in form. We have checked for a few cases that a full unfolding procedure applied to the measured $dN/\Delta\phi$ distributions using singular value decomposition regularization of the response matrix reproduces the correction in Eq. (12). From the corrected ratios, $R^{\rm cor}(\Delta\phi_i, p_T)$, we use Eq. (10) to obtain $R_{\rm AA}(\Delta\phi_i, p_T)$.

IV. RESULTS

A. Elliptic flow coefficient

The results of the v_2 measurements using the methods described in Sec. III D are presented in Fig. 4 as a function of p_T for different centrality bins. The data points in the figure are plotted at the mean $\pi^0 p_T$ in bins of width $\Delta p_T = 0.5$ GeV/c for $p_T < 4$ GeV/c and $\Delta p_T = 1$ GeV/c for $p_T > 4$ GeV/c. The error bars shown on the v_2 data points were obtained by multiplying the raw v_2 fit errors (see Sec. III D) by the same reaction plane resolution correction factor applied to the v_2 values themselves. The error bars, then, represent uncorrelated statistical errors on the measured v_2 values arising from statistical errors on the $dN/d\Delta\phi$ data points used in the fits (these errors would be categorized as Type A uncertainties in the framework described in Ref. [44] or p_T uncorrelated). Systematic errors on the v_2 measurements due to the reaction plane determination procedure and from systematic uncertainties in the reaction plane resolution correction are represented in Figs. 4 and 5 by filled boxes, which for most data points are similar in size or smaller than the data points (these uncertainties are classified as Type B [44] or p_T correlated).

Figure 5 shows $v_2(p_T)$ for four centrality ranges, obtained by combining data from the centrality bins shown in Fig. 4. The corrected $dN/d\Delta\phi$ distributions from individual centrality bins were summed over a given centrality range and then fit to obtain the corrected v_2 values shown in Fig. 5. The reaction plane resolution correction produces correlated errors in the corrected $dN/d\Delta\phi$ distributions for each original centrality bin, and these correlated errors persist in the summed $dN/d\Delta\phi$ distribution. These correlated errors are not included in the statistical errors for the fit to the combined $dN/d\Delta\phi$ distribution, but their impact on the final v_2 value is estimated separately by evaluating the changes in the v_2 fit parameter that result from adding to the summed $dN/d\Delta\phi$ values $\pm 1\sigma$ of the correlated errors. Because this estimated uncertainty results from the statistical uncertainties on the v_2 values for the original centrality bins, we include the 1σ bounds obtained from this procedure in the statistical error on the v_2 values for the combined centrality bins. Systematic errors for the combined bins are plotted similarly to those in Fig. 4.

The results presented here nearly double the p_T range of previous PHENIX $\pi^0 v_2$ measurements from RHIC Run-2 [25]. Those measurements are shown for comparison purposes in Fig. 5. Good agreement is seen between the Run-4 measurements presented here and the Run-2 results except in

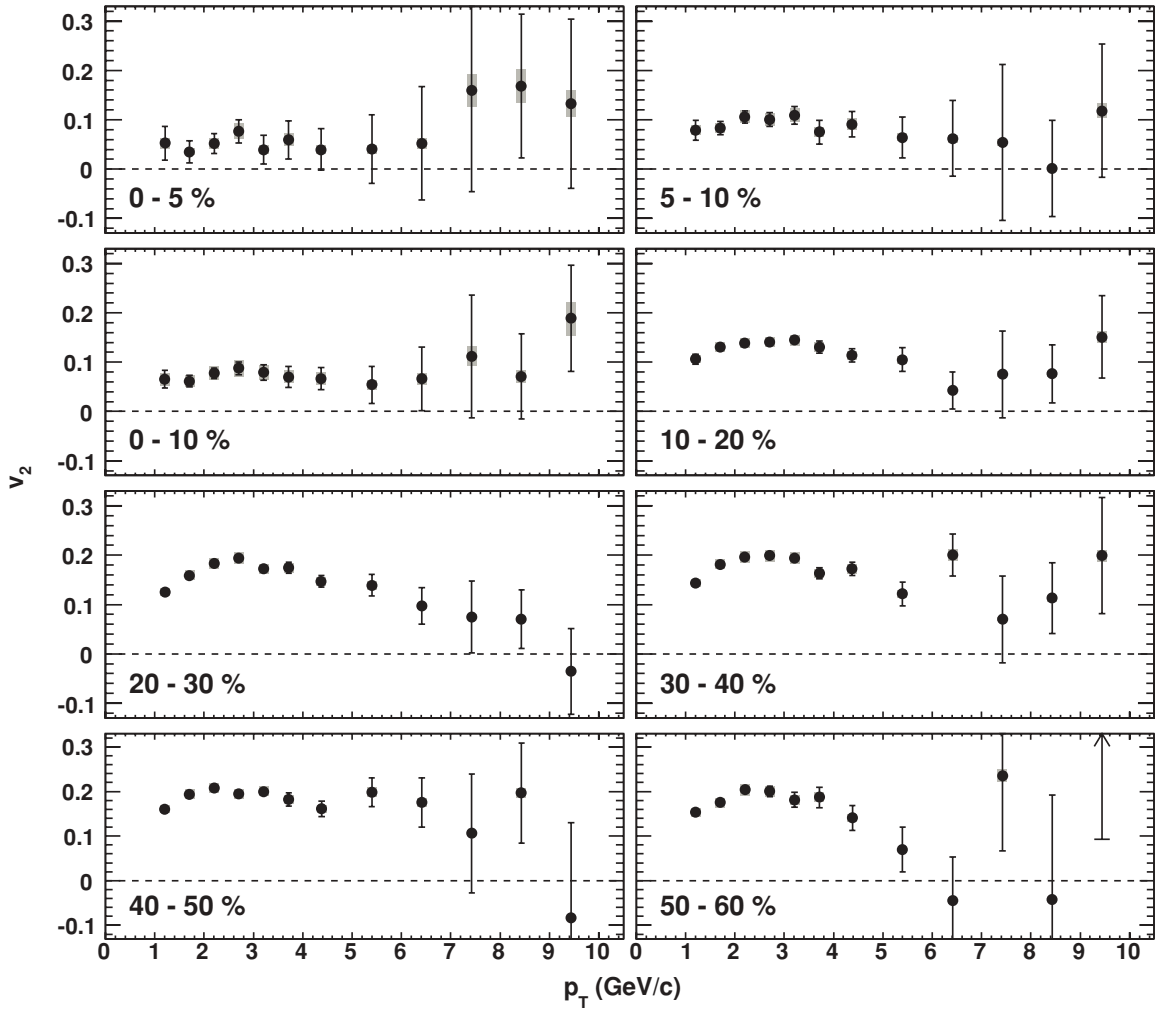

FIG. 4. π^0 v_2 versus p_T for centralities 0–5%, 5–10%, 0–10%, 10–20%, 20–30%, 30–40%, 40–50%, and 50–60%. The arrow in the 50–60% panel shows the lower limit of the uncertainty on the data point, which lies outside the bounds of the plot.

the 40–60% centrality bin where the new v_2 measurements are systematically higher by ~30%. This difference is attributed to improved reaction plane resolution corrections for the 40–60% centrality bin resulting from the combining of *corrected* $dN/\Delta\phi$ distributions from smaller centrality bins. This summing procedure better handles the rapid variation of reaction plane resolution with centrality in midcentral to peripheral collisons. Furthermore, we have cross-checked the procedure using 5% bins, verifying that the combined result reproduces the data analyzed in wider bins. The previous Run-2 analysis did not have a sufficiently large data sample to allow the use of separate 40–50% and 50–60% bins, and therefore the reaction plane resolution correction was necessarily less accurate. The measured v_2 values presented in Fig. 4 and Fig. 5 are also consistent with previously published PHENIX charged pion v_2 measurements [14,25].

The results in Figs. 4 and 5 show a rapid increase of v_2 with increasing p_T at low p_T, a maximum in the range $2 < p_T < 3$ GeV/c, and then at higher p_T a decrease of v_2 with increasing p_T. An increase in v_2 at low p_T is well established [45–47] and is understood to result from the collective elliptic flow of the medium generated by the initial spatial anisotropy of the collision zone. Hydrodynamical models have been successful in quantitatively describing the pion $v_2(p_T)$ in the region $p_T < 1.5$ GeV/c. However, it has also been well established that the pion $v_2(p_T)$ deviates from the hydrodynamic prediction above 1.5 GeV/c, a result that is understood to imply the contribution of hard processes, distortions of the spectrum due to recombination at freeze-out, and/or effects from dispersive hadronic evolution after freeze-out. Thus, a change in the variation of v_2 with p_T near $p_T \sim 2$ GeV/c is not unexpected. If the large v_2 values at lower p_T are interpreted as resulting from soft, collective mechanism, then a decrease in v_2 for $p_T > 3$ GeV/c suggested by the data in Fig. 4 would naturally reflect an increasing contribution of hard processes with smaller v_2.

To statistically test the significance of the decrease of v_2 with p_T, we show in Fig. 6 the results of linear fits to the high-p_T v_2 values for the 20–30% and 30–40% centralities. The panels on the left-hand side of Fig. 6 display a series of fits beginning at higher p_T values, the first fit starting at the p_T near the maximum v_2, $p_T = 2.5$ GeV/c. The right-hand

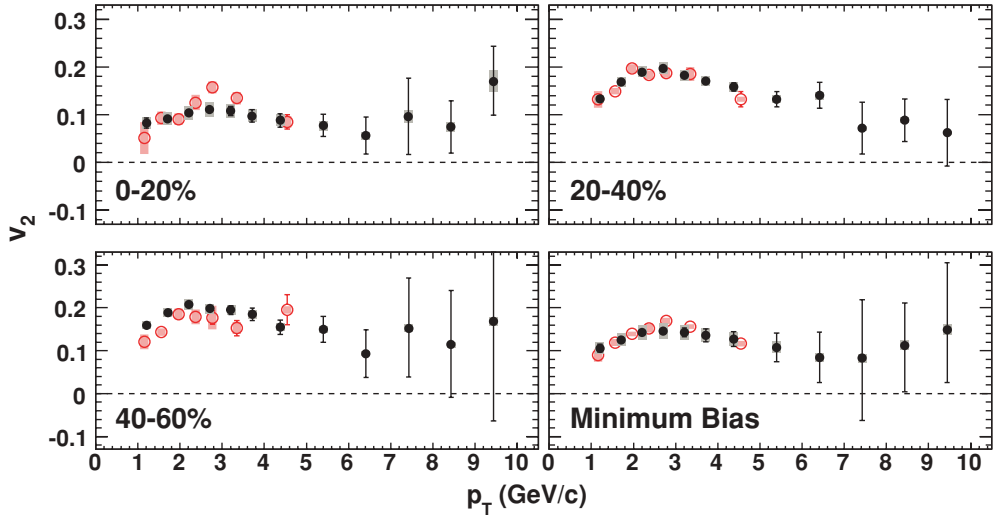

FIG. 5. (Color online) π^0 v_2 versus p_T for centralities 0–20%, 20–40%, 40–60% and minimum bias. The closed (black) circles are data presented in this article, and the open (red) circles are previously published results [25].

panels show the 1σ limits of the functions for the three fits in the series, calculated from the 1σ variation of the two fit parameters (and including the covariance between them). The results of the fits indicate that the decrease of v_2 with p_T at higher p_T is statistically significant, though the data points for $p_T > 5$ GeV/c are not sufficient by themselves to establish a trend. We can state, however, that the points for $p_T > 5$ GeV/c are consistent with the linear decrease obtained including the lower-p_T points. A question we would like to answer, then, is whether the data show any indications of devation from a monotonic decrease in $v_2(p_T)$ indicating the transition to a quenching-dominated azimuthal variation. The v_2 at low p_T follows from primordial source geometry and density distribution, causing the hydrodynamic pressure gradients to be steeper in plane than out of plane: hence an anisotropic momentum distribution arises. At high p_T, a completely unrelated phenomenon—high-p_T parton in-medium attenuation—leads to a similar momentum space anisotropy. This is an influence of primordial collision geometry, as hadron suppression is smaller in plane than out of plane. This also creates a positive v_2 that, however, reflects different physics.

A complete understanding of $v_2(p_T)$ over the measured p_T range therefore requires the treatment of the transition from soft to hard dominated physics. According to the above

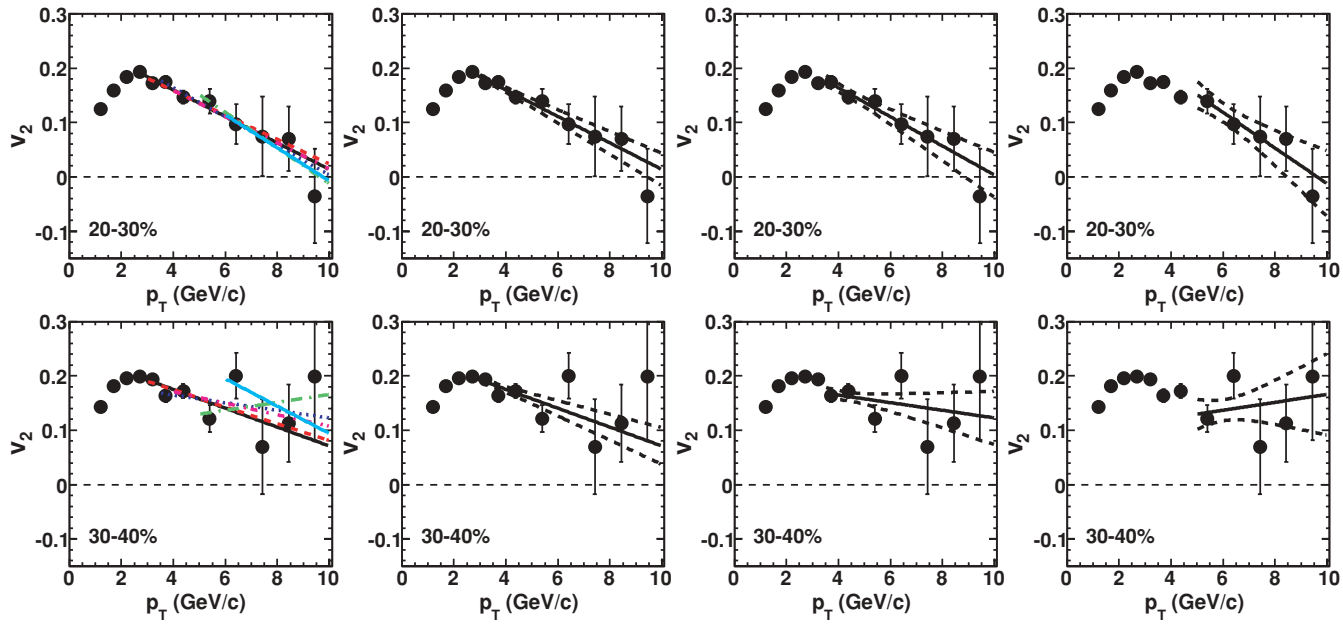

FIG. 6. (Color online) v_2 versus p_T for 20–30% and 30–40% centralities, with fits of the high-p_T data to a first-order polynomial. From right to left, the first panel shows the series of fits, with each fit starting with a successively higher p_T. The second, third, and fourth panels show selected fits with uncertainty bands based on the 1σ variation of the fit parameters, including their covariance.

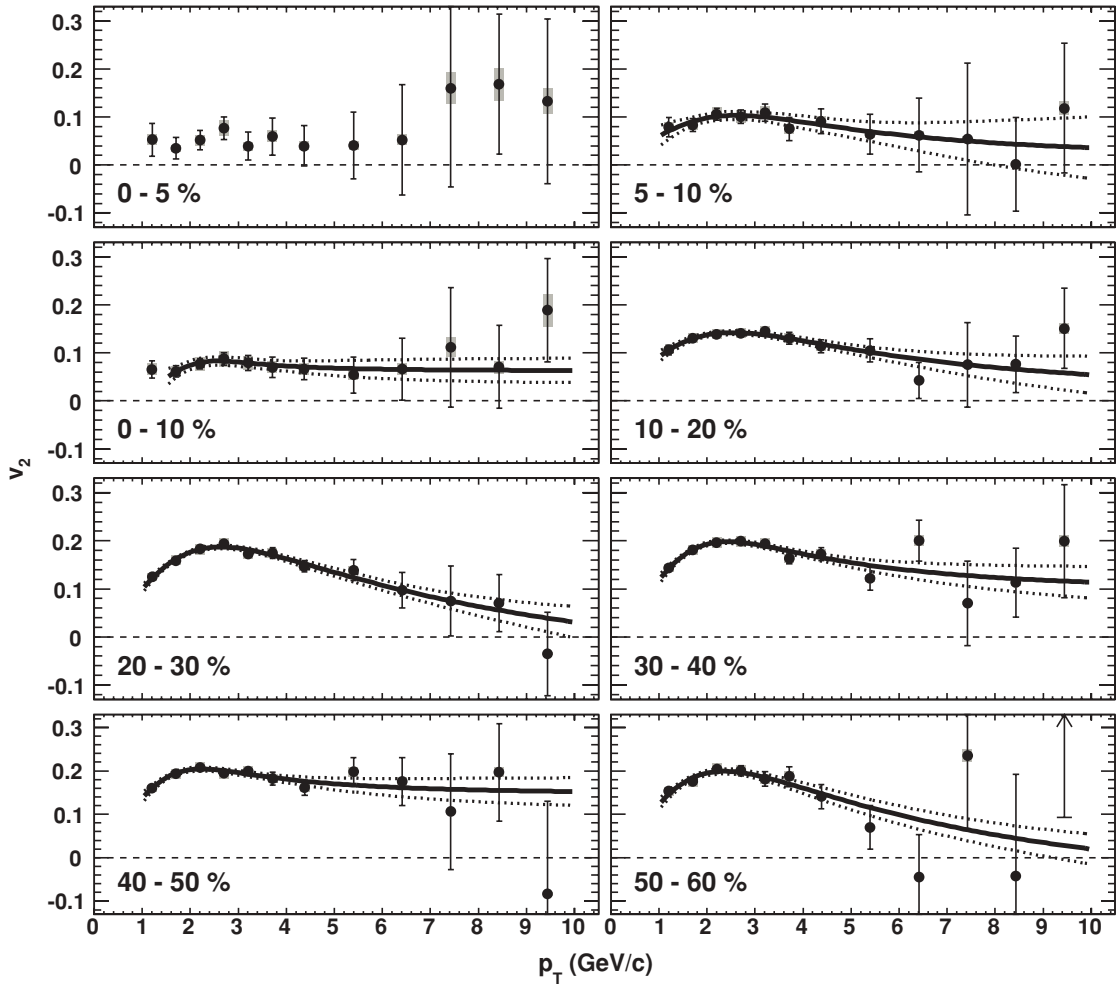

FIG. 7. π^0 v_2 versus p_T for centralities 0–5%, 5–10%, 0–10%, 10–20%, 20–30%, 30–40%, 40–50%, and 50–60%. The arrow in the 50–60% panel shows the lower limit of the uncertainty on the data point, which lies outside the bounds of the plot. The solid lines represent the fit to the data, Eq. (13). The dashed lines represent the 1σ deviations of the fit function. See text for more details.

discussion, in the p_T range where v_2 is maximum, particle production is likely not dominated by hard processes and the reduction of v_2 with increasing p_T indicates increasing hard-scattering contributions (or decreasing soft contamination). Motivated by this general argument, we have attempted to describe the results in Figs. 4 and 5 by a functional form

$$v_2(p_T) = \left[\frac{(p_T/\lambda)^m}{1+(p_T/\lambda)^m}\right]\left(a + \frac{1}{{p_T}^n}\right). \qquad (13)$$

The first term is intended to describe a rapidly rising and saturating soft v_2 resulting from collective motion while the second term represents a rapidly falling soft/hard ratio. The additive constant in the second term represents an asymptotic v_2 that could describe a constant or slowly varying azimuthal-dependent quenching. We show in Figs. 7–8 the optimum fits to the full set of $v_2(p_T)$ values in the different centrality bins and the result of 1σ variation of the fit parameters taking into account the complete covariance matrix from the fits.

The fits to the data show that the measured p_T dependence of the $\pi^0 v_2$ is qualitatively compatible with a description of the low- and intermediate-p_T region in terms of a collective flow modulation diluted by a decreasing relative soft contribution with increasing p_T. Assuming this picture, it is then important to determine at what p_T the contamination from the soft production no longer dominates the measured $\Delta\phi$ variation of π^0 yield. For most of the centrality bins, the fits suggest that v_2 decreases over most of the measured p_T range albeit with a decreasing slope at higher p_T. The central bins are compatible with v_2 continuing to decrease beyond the measured p_T range although the 1σ uncertainty bands also accommodate v_2 saturating within the measured range. The more peripheral bins (30–40% and 40–50%) suggest that the v_2 has reached a nearly p_T-independent value by $\sim$5 GeV/c. The 50–60% centrality bin has sufficient fluctuations that little can be inferred from the p_T dependence of v_2 in that centrality bin. In all of the centrality bins, the data are consistent with a smooth reduction of $v_2(p_T)$ from a maximum to a nonzero value at high p_T with that value increasing in more peripheral collisions as would be expected from quenching in an increasingly anisotropic medium. While the functional form in Eq. (13) can describe the p_T variation of v_2 within the range of the current data and within the statistical fluctuations of the data points, it

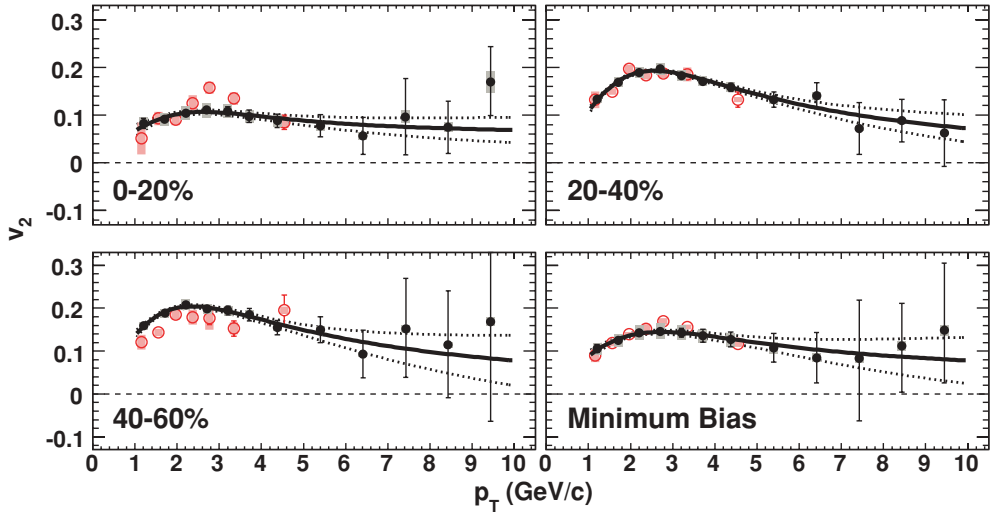

FIG. 8. (Color online) π^0 v_2 versus p_T for centralities 0–20%, 20–40%, 40–60% and minimum bias. The closed (black) circles are data presented in this article, and the open (red) circles are previously published results [25]. The solid and dashed lines as in Fig. 7.

is possible that this description will fail at higher p_T with improved statistics. In fact, a statistically significant deviation of $v_2(p_T)$ from the form in Eq. (13) might provide the most direct evidence of the dominance of quenching effects in determining v_2.

B. Nuclear modification factor with respect to the reaction plane

The nuclear modification factor as a function of $\Delta\phi$ for six centrality bins is shown in Figs. 9–14. The closed circles represent the $\Delta\phi$-dependent measurements described in this article while the open circles positioned at $\Delta\phi = \pi/4$ represent the inclusive R_{AA} measurement [20]. In both cases statistical uncertainties (i.e., Type A) are represented by the error bars. For the inclusive R_{AA} measurement, the total systematic uncertainties (or Type C [44]) are shown by the boxes. The upper and lower 1σ ranges of the correlated statistical uncertainties (i.e., Type B) on the $R_{AA}(\Delta\phi)$ measurements resulting from the reaction plane resolution correction are shown by the (blue) solid and (red) dashed lines. For all bins except the 0–10% centrality bin a dotted line is plotted at $R_{AA} = 1$ for reference. We note that by construction, the average $R_{AA}(\Delta\phi)$ from the reaction plane dependent measurements must be equal to the inclusive R_{AA}.

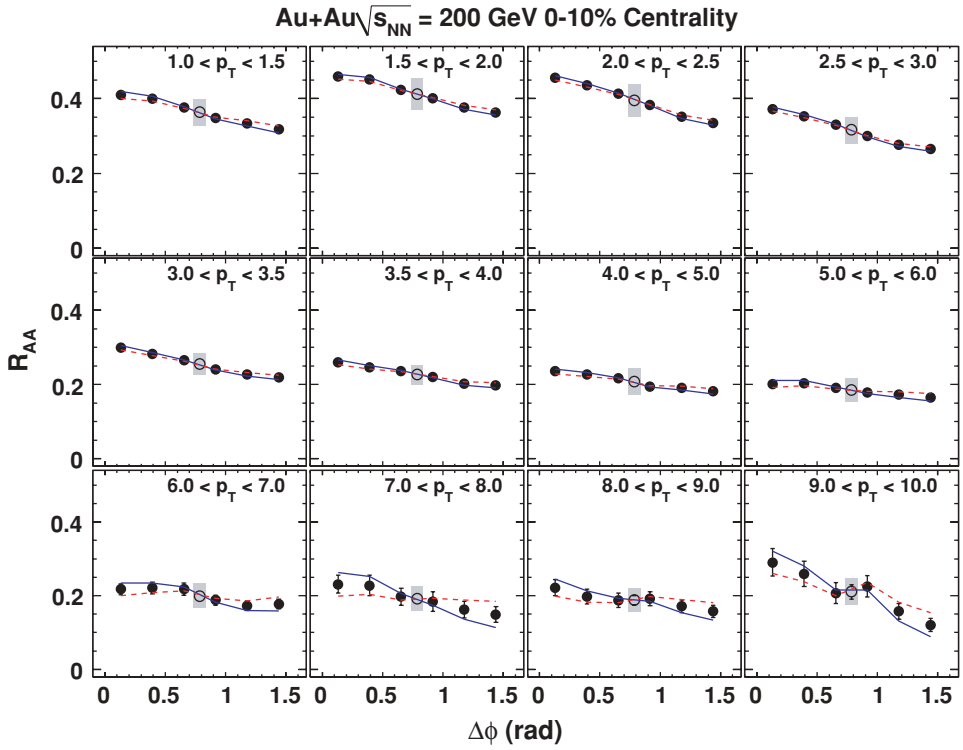

FIG. 9. (Color online) π^0 R_{AA} versus angle of emission with respect to the reaction plane for 0–10% centrality. The error bars denote the statistical errors, while the solid (blue) line and dashed (red) line represent the systematic error due to the resolution correction factor. The inclusive R_{AA} measurement is shown with the open circle, for which the error bar shows the statistical error and the box shows the systematic error.

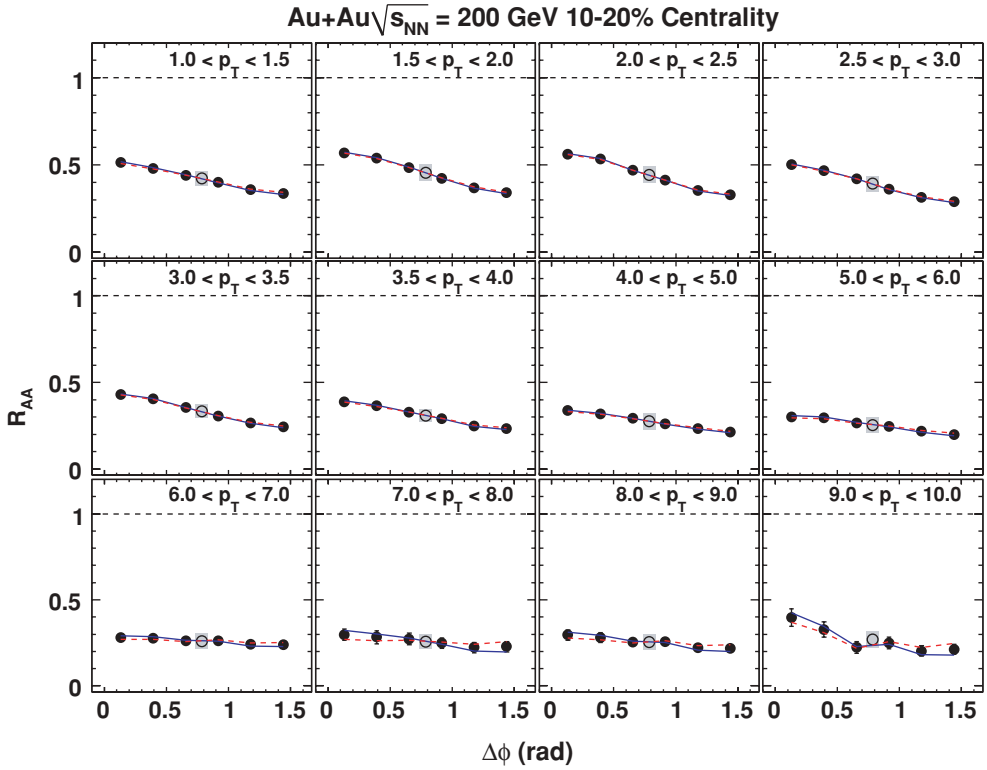

FIG. 10. (Color online) π^0 R_{AA} versus angle of emission with respect to the reaction plane for 10–20% centrality. Colors/data points as in Fig. 9.

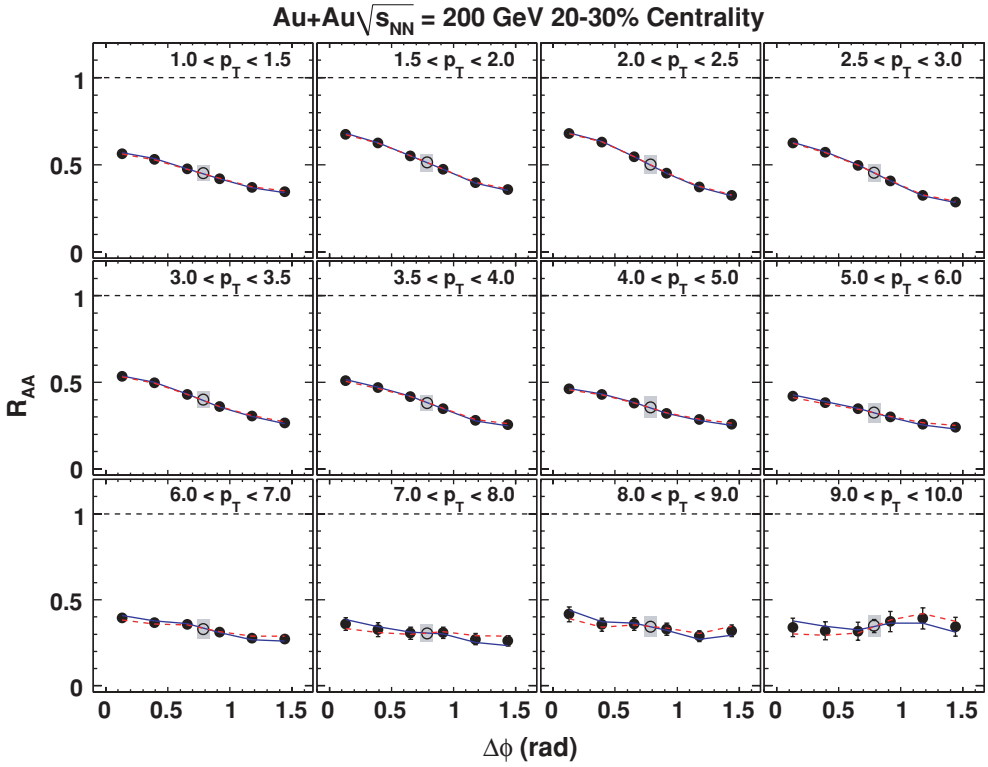

FIG. 11. (Color online) π^0 R_{AA} versus angle of emission with respect to the reaction plane for 20–30% centrality. Colors/data points as in Fig. 9.

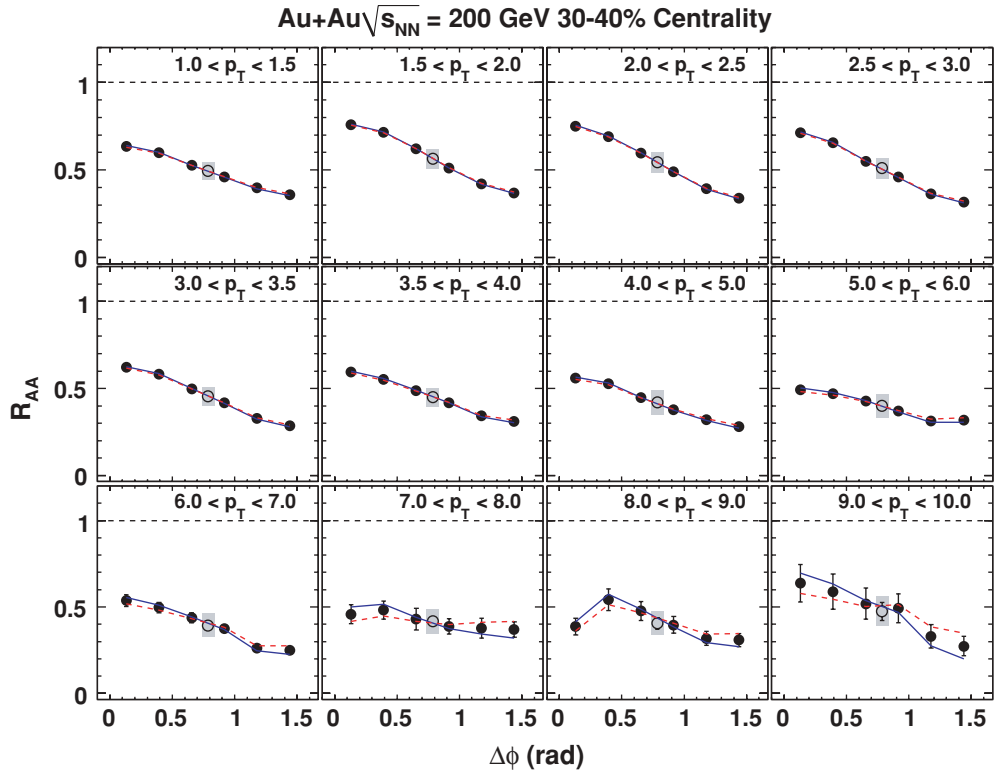

FIG. 12. (Color online) π^0 R_{AA} versus angle of emission with respect to the reaction plane for 30–40% centrality. Colors/data points as in Fig. 9.

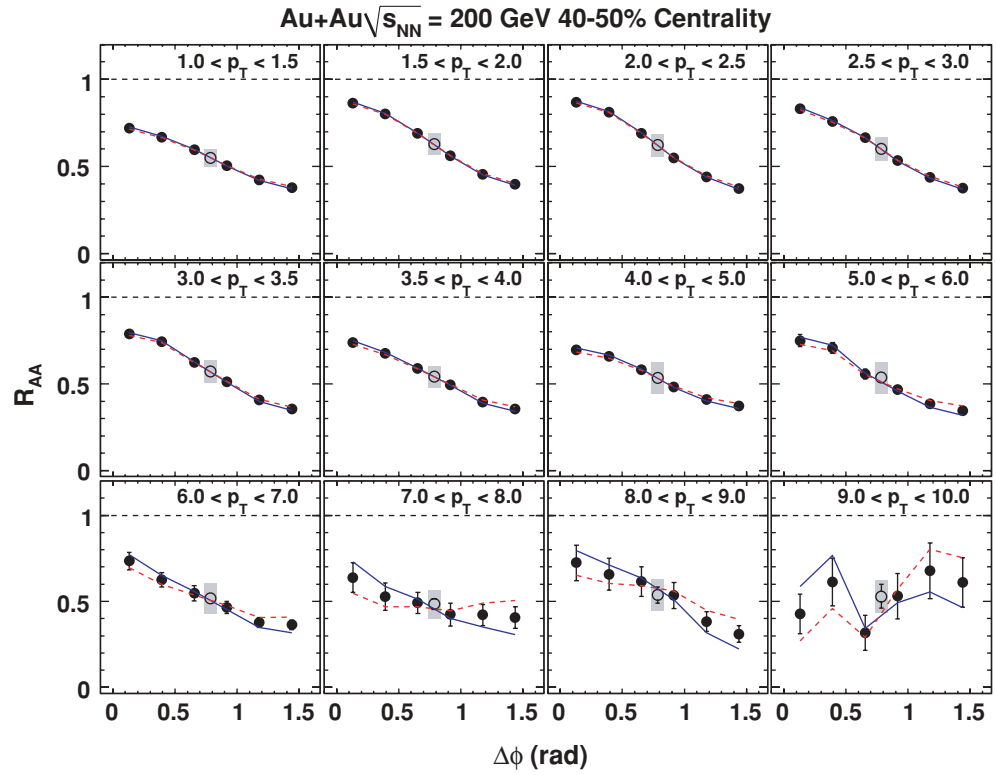

FIG. 13. (Color online) π^0 R_{AA} versus angle of emission with respect to the reaction plane for 40–50% centrality. Colors/data points as in Fig. 9.

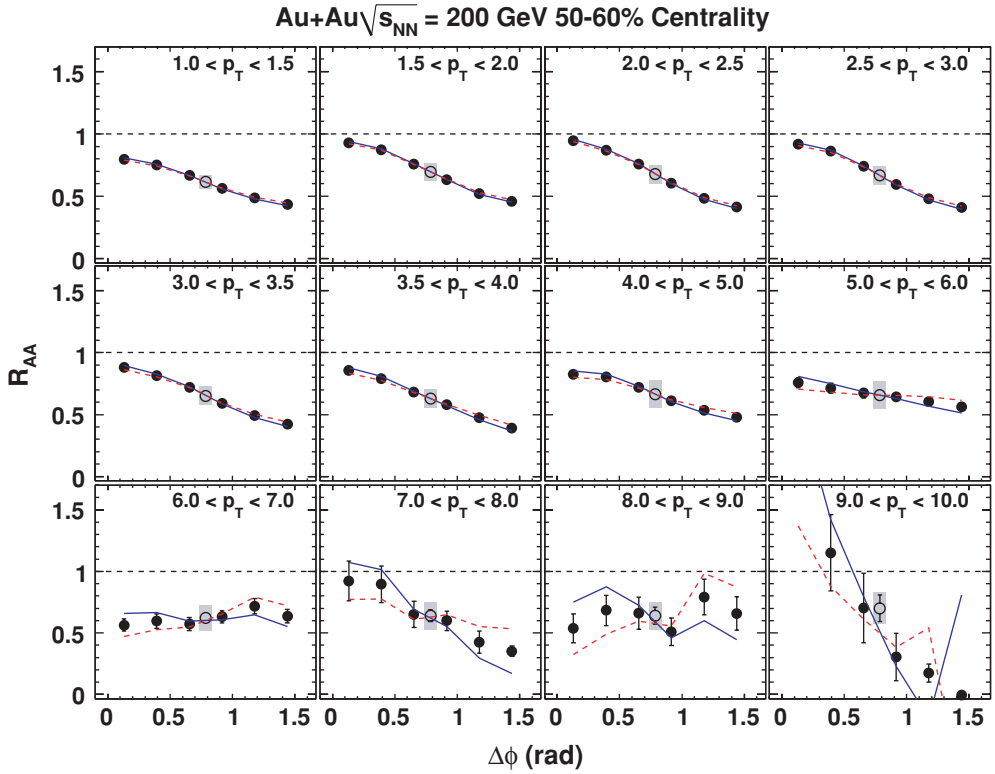

FIG. 14. (Color online) π^0 R_{AA} versus angle of emission with respect to the reaction plane for 50–60% centrality. Colors/data points as in Fig. 9.

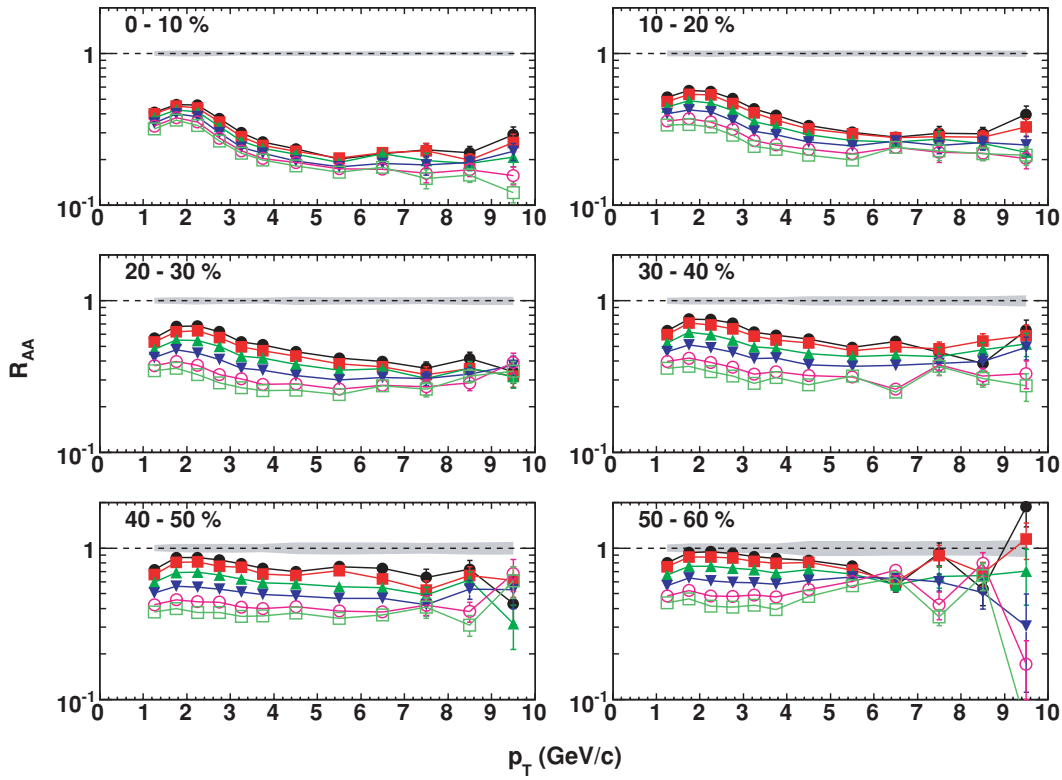

FIG. 15. (Color online) Semilog plots of $R_{AA}(p_T)$ for each $\Delta\phi$ bin in different centrality ranges. The $\Delta\phi$ bins are represented as follows: closed (black) circles, 0–15°; closed (red) squares, 15–30°; closed (light green) triangles, 30–45°; closed inverted (blue) triangles, 45–60°; open (magenta) circles, 60–75°; and open (dark green) squares, 75–90°. The systematic error in the inclusive R_{AA} is represented by the gray bands. Errors due to the correction factor have been omitted for clarity.

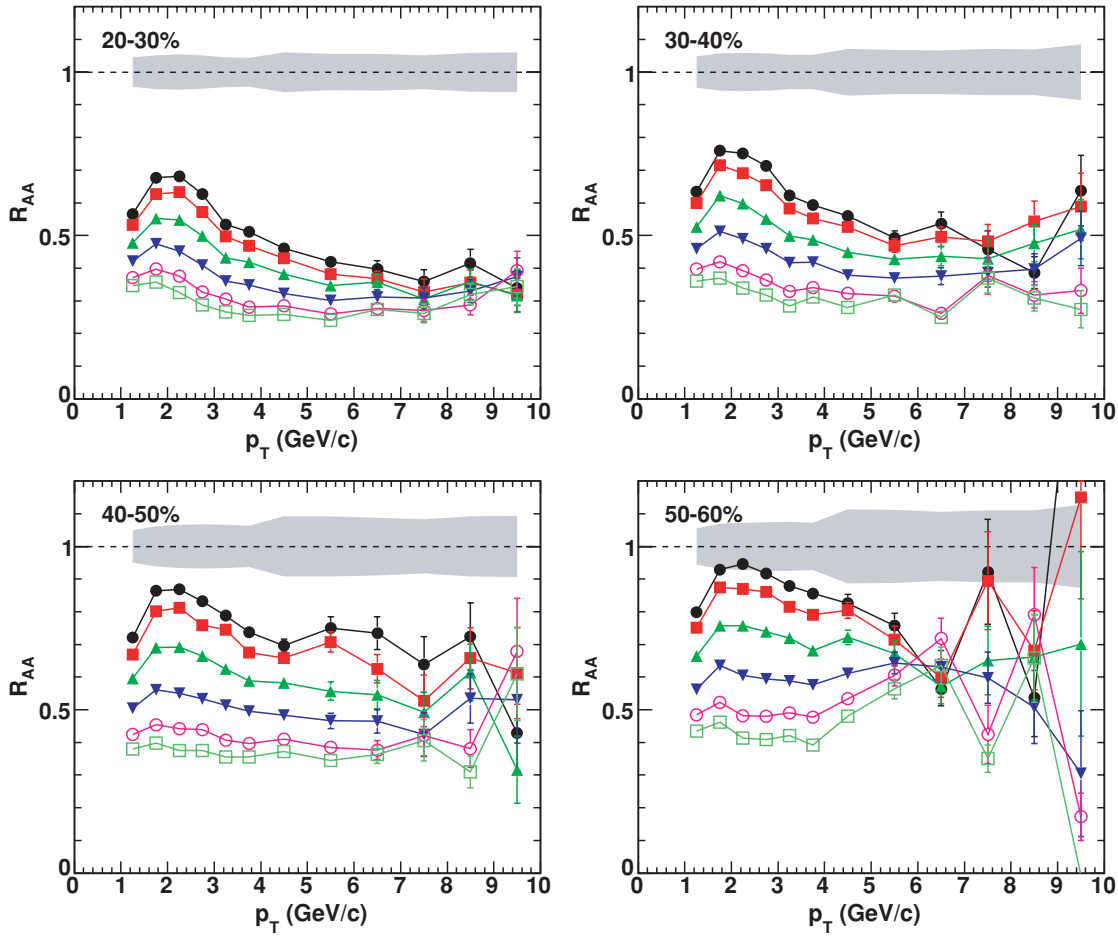

FIG. 16. (Color online) $R_{AA}(p_T)$ for different $\Delta\phi$ bins in the 20–30%, 30–40%, 40–50%, and 50–60% centrality ranges. Colors/data points as in Fig. 15.

The results in the Figs. 9–14 show that the in-plane π^0 suppression is generally weaker and varies more rapidly with p_T than the suppression for π^0s produced at larger angles. As the collisions become more peripheral (for example, 50–60%), the small suppression seen in the inclusive R_{AA} almost vanishes for π^0s emitted close to the reaction plane. In a previous analysis [34], it was observed that the in-plane R_{AA} even exceeded unity for peripheral collisions; these data exhibit no such enhancement. However, the results presented in this article agree within systematic errors with previously reported data.

The $R_{AA}(\Delta\phi)$ results are combined in Fig. 15 that shows the p_T dependence of the R_{AA} in each of the six $\Delta\phi$ bins included in this analysis. We use a semilog scale so that the reduction of the $\Delta\phi$-integrated R_{AA} in more central collisions does not confuse the interpretation of the results. For clarity, the results from the 20–30%, 30–40%, 40–50%, and 50–60% centrality bins are shown on linear plots in Fig. 16.

The $R_{AA}(p_T)$ results exhibit a peak near 2 GeV/c, which becomes more prominent for more central collisions. The peak is strongest in the 0–10% bin where there is little modulation of the $\Delta\phi$ distributions at low or high p_T, so the peak cannot be directly attributed to elliptic flow. The peak in R_{AA} near 2 GeV/c is much weaker in the more peripheral (40–50% and 50–60%) centrality bins, particularly for π^0s produced at larger $\Delta\phi$, and the primary variation seen in these peripheral bins with increasing $\Delta\phi$ is a reduction in R_{AA} that is only weakly p_T dependent.

For the intermediate centrality bins (10–20% through 30–40%) the peaking in R_{AA} is seen in all $\Delta\phi$ bins but is much stronger in the in-plane bins. For these intermediate centralities and for p_T values above the peak in R_{AA} ($p_T \gtrsim 3$ GeV/c), the R_{AA} for π^0s produced at angles normal to the reaction plane is nearly constant with p_T while the R_{AA} for π^0s produced at small angles from the reaction plane decreases rapidly with increasing p_T. The near constancy of the out-of-plane R_{AA} together with the rapid reduction of the in-plane R_{AA} indicates that in the intermediate centrality bins, the v_2 and inclusive R_{AA} decrease simultaneously with increasing p_T such that $R_{AA}(\pi/2, p_T) = R_{AA}(p_T)(1 - 2v_2)$ is approximately constant. We will argue below that a correlation between R_{AA} and v_2 may naturally result from the underlying physics responsible for the azimuthal variation of the particle yields. However, we observe that a simultaneous reduction in integrated R_{AA} and v_2 suggested by the more central $R_{AA}(p_T)$

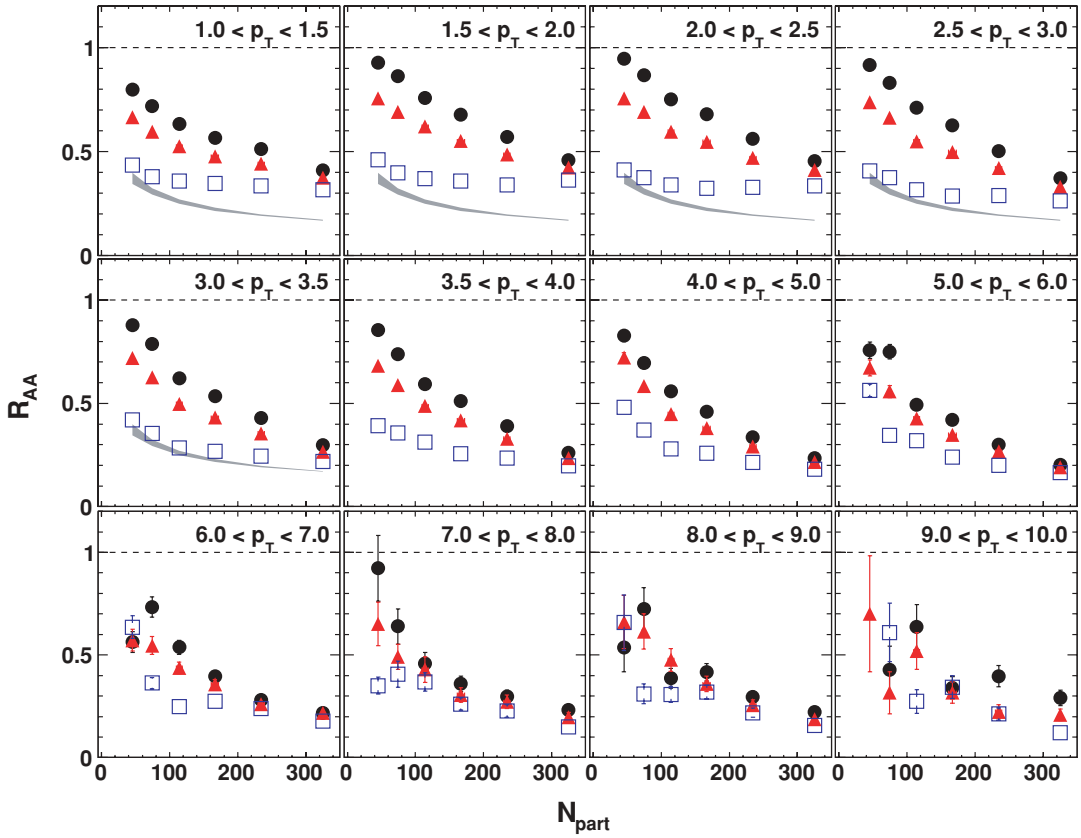

FIG. 17. (Color online) π^0 $R_{\rm AA}(N_{\rm part})$ in reaction-plane bins at fixed p_T. The three bins are as follows: closed (black) circles are $R_{\rm AA}(0 < \Delta\phi < 15^\circ)$ (in plane), the closed (red) triangles are the $R_{\rm AA}(30 < \Delta\phi < 45^\circ)$, and open (blue) squares are $R_{\rm AA}(75 < \Delta\phi < 90^\circ)$ (out of plane). The curves are the $R_{\rm AA}$ values expected from $N_{\rm part}$ scaling, using values of $N_{\rm part}$ and $N_{\rm coll}$ calculated from the Glauber model [48].

data would be contrary to naive energy-loss expectations because smaller $R_{\rm AA}$ would imply stronger quenching in the medium that would, in turn, imply larger variation between in-plane and out-of-plane quenching.

A similar implicit correlation between integrated $R_{\rm AA}$ and v_2 is seen in the centrality dependence of the $R_{\rm AA}(\Delta\phi)$ results. These are replotted in Fig. 17 as a function of $N_{\rm part}$ for three $\Delta\phi$ bins—the bins closest to and farthest from the reaction plane and one of the intermediate bins. In addition, the expectation for $N_{\rm part}$ scaling (a calculation based on the Glauber model [48]) is shown for the lowest-p_T bins. For $N_{\rm part} > 100$, the out-of-plane $R_{\rm AA}$ values are nearly independent of centrality while the in-plane $R_{\rm AA}$ values decrease rapidly with increasing centrality. This result would have a natural geometric interpretation for π^0 production dominated by hard scattering and jet quenching. The length of the medium normal to the reaction plane varies only slowly with centrality except in the most peripheral collisions. Then, if the π^0 suppression is determined primarily by the path length of its parent parton in the medium, the $\pi^0 R_{\rm AA}$ would be nearly constant. Following the same argument, the yield for pions in the direction of the reaction plane would be much less suppressed in noncentral collisions due to the short path lengths of the parent partons in the medium. However, with increasing centrality and decreasing anisotropy of the collision zone, the in-plane parton path lengths would grow to match those in the out-of-plane direction. Thus, if the π^0 suppression depended primarily on path length, the in-plane $R_{\rm AA}$ would naturally drop to match the out-of-plane values reproducing the behavior of Fig. 17. To better see the difference between the in- and out-of-plane behaviors, these data are also plotted on Fig. 18 with a semilog scale.

One difficulty with this geometric interpretation of the $R_{\rm AA}(\Delta\phi)$ results given above is that the trend in the data that it is supposed to explain persists down to low p_T, where the v_2 values are too large to be accounted for via perturbative or formation-time-based energy-loss scenarios [26–30,49]. That fact coupled with the pronounced peaking in $R_{\rm AA}(\Delta\phi)$ near 2 GeV/c suggests that physics other than hard scattering and jet quenching must be invoked to explain the π^0 yields at intermediate p_T. However, the fact that the out-of-plane yields show less pronounced peaking near 2 GeV/c, that they vary little as a function of p_T above 3 GeV/c, and that they vary little with centrality for $N_{\rm part} > 100$ could be interpreted to imply that the π^0 suppression at angles normal to the reaction plane more directly represents the effects of quenching of hard quarks and gluons while the yield of π^0s produced more closely aligned with the reaction plane is enhanced by the

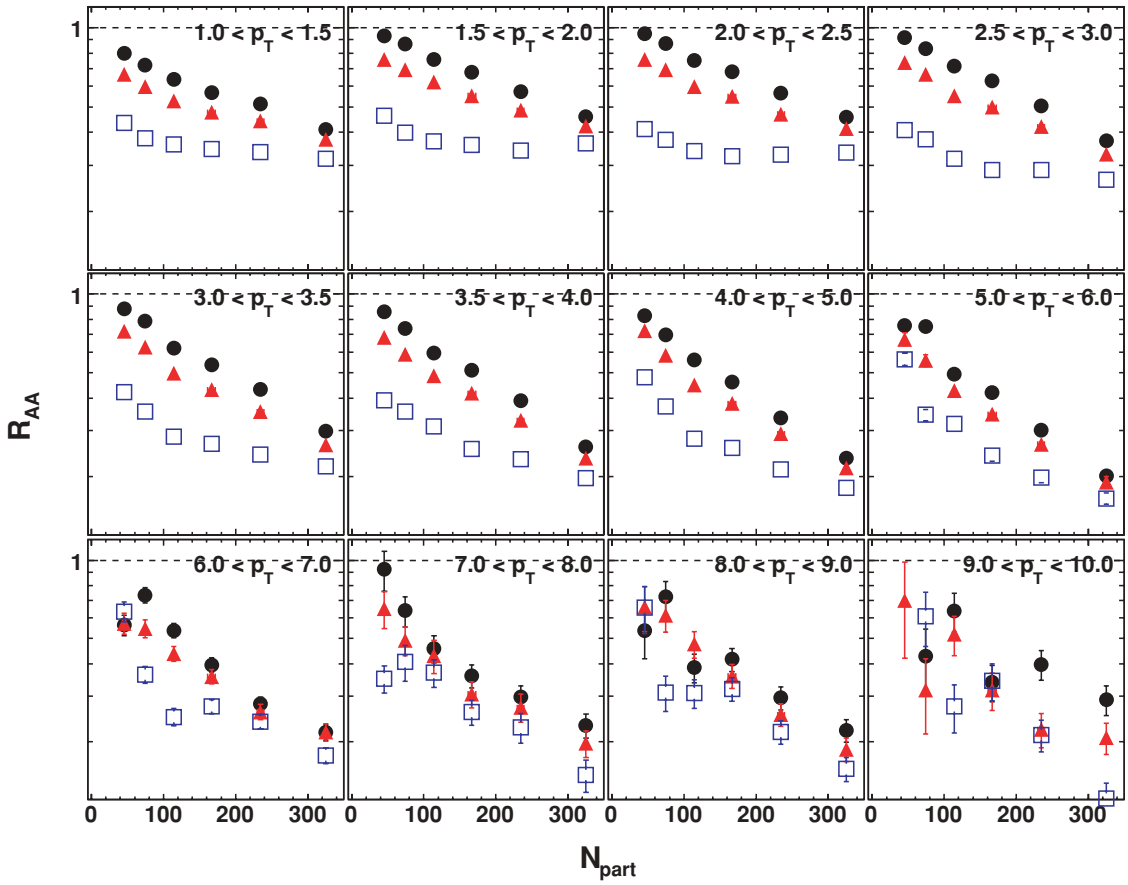

FIG. 18. (Color online) π^0 $R_{\rm AA}(N_{\rm part})$ in reaction-plane bins at fixed p_T, with log scale on the y axis. Colors/data as in Fig. 17.

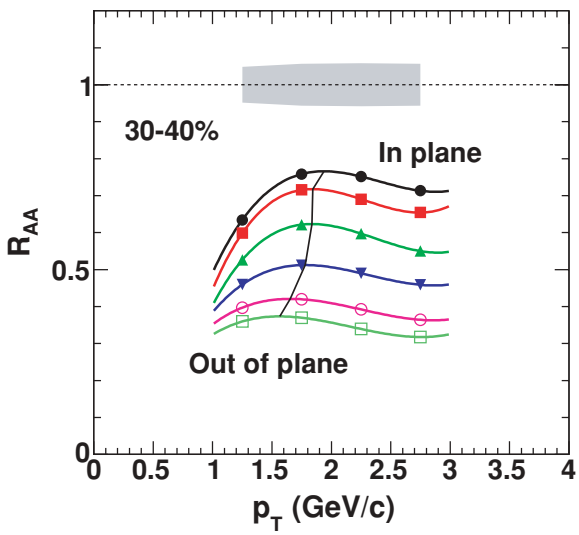

FIG. 19. (Color online) Illustration of the shift in the peak positions in $R_{\rm AA}(p_T)$ for the 30–40% centrality bin. Colors/data points as in Fig. 15.

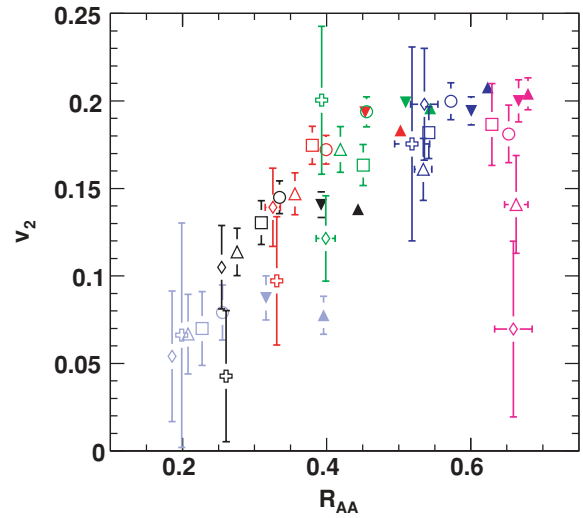

FIG. 20. (Color online) π^0 v_2 vs. inclusive $R_{\rm AA}$. The points denote bins in p_T as follows: triangles $2 < p_T < 2.5$ GeV/c, inverted triangles $2.5 < p_T < 3$ GeV/c, circles, $3 < p_T < 3.5$ GeV/c; squares, $3.5 < p_T < 4$ GeV/c; open triangles, $4.0 < p_T < 4.5$ GeV/c; diamonds, $4.5 < p_T < 5$ GeV/c; crosses, $5 < p_T < 6$ GeV/c. Centrality bins are indicated by the colors: light blue, 0–10%; black, 10–20%; red, 20–30%; green, 30–40%; blue, 40–50%; magenta, 50–60%.

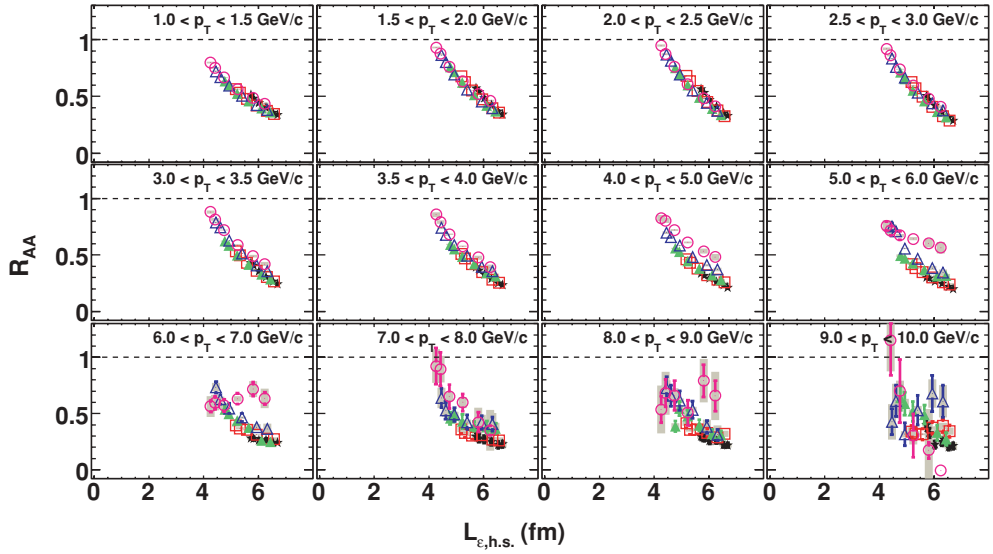

FIG. 21. (Color online) π^0 $R_{\rm AA}$ versus L_ϵ based on the hard sphere calculation. Each panel corresponds to a p_T bin. Each data point corresponds to a particular centrality bin and $\Delta\phi$ value. The centralities are represented as follows: (black) stars, 10–20%; open (red) squares, 20–30%; (green) triangles, 30–40%, open (blue) triangles, 40–50%; open (magenta) circles, 50–60%. The height of the boxes represent the systematic errors on $R_{\rm AA}$ for the corresponding L_ϵ.

collective motion of the system. That additional enhancement could either be due to soft hadrons being boosted to larger p_T values by the collective elliptic flow or could result from weaker quenching for partons moving in the direction of the flow field [27,50]. Simultaneous description of the in-plane and out-of-plane behavior is a sensitive test of energy-loss models.

In the context of the above arguments, it may be worth considering the possible role of more mundane "geometry" on the evolution of $R_{\rm AA}$ with p_T and $N_{\rm part}$. Namely, at low p_T particle production is known to increase proportionally to $N_{\rm part}$ not $N_{\rm coll}$, so there is a natural reason for $R_{\rm AA}$ to be less than unity at low p_T. In the absence of quenching, then, the $R_{\rm AA}$ would increase to 1 or above. Naively, the peak observed in $R_{\rm AA}(p_T)$ might be interpreted as resulting from a contribution of hard processes that is quenched more strongly with increasing p_T. The role of soft production would also presumably be reflected in the $N_{\rm part}$ evolution of $R_{\rm AA}$ in the lowest-p_T bins. However, while such analysis in terms of an evolution from soft to hard physics is compelling, it does not fit with the data presented in this article.

In Fig. 17 the gray bands included in the five lowest-p_T bins show the $R_{\rm AA}$ values that would result if particle production increased proportionally to $N_{\rm part}$. The $R_{\rm AA}$ values in the lowest-p_T bins are not well described by the gray bands, even for out-of-plane production, which has the lowest $R_{\rm AA}$ values. All of the measured $R_{\rm AA}$ values are much larger than could be explained by the $N_{\rm part}$ scaling; the $R_{\rm AA}$ values for pions produced in the reaction plane differ from the $N_{\rm part}$ expectation by a factor of 2. Of course, at the lowest p_T we expect the reaction plane dependence of the yields to be a result of elliptic flow that boosts the p_T of the particles with a larger boost for smaller $\Delta\phi$. That boost will necessarily increase $R_{\rm AA}$ above the naive $N_{\rm part}$ expectation. But the elliptic flow is a modulation on an overall radial flow pattern that will also boost particles moving normal to the reaction plane, increasing the $R_{\rm AA}$ above the $N_{\rm part}$ expectation even for particles produced out of plane. Our data suggest that collective physics plays a dominant role at intermediate p_T, in the region where both v_2 and $R_{\rm AA}(p_T)$ reach a maximum.

The v_2 values presented in Figs. 7–8 also peak near 2 GeV/c, but the locations of the maxima in v_2 are shifted to higher p_T than the maxima in $R_{\rm AA}(\Delta\phi)$. This suggests that the two effects may not be directly related, but we observe that the maxima in the $R_{\rm AA}(p_T)$ distributions in Figs. 15–16 shift to larger p_T for smaller $\Delta\phi$. To better illustrate the shift of the maxima in $R_{\rm AA}(p_T)$ we show in Fig. 19 the $R_{\rm AA}(p_T)$ values for the different $\Delta\phi$ bins and indicate the variation of the peak position obtained using polynomial fits to the first four p_T bins. For the 30–40% centrality bin, the maximum in $R_{\rm AA}(p_T)$ for $\Delta\phi < \pi/12$ is shifted by 0.4 GeV/c relative to the $5\pi/12 < \Delta\phi < \pi/2$ bin. This shift in the peak $R_{\rm AA}(p_T)$ with $\Delta\phi$ can produce a $v_2(p_T)$ that peaks higher in p_T than the inclusive $R_{\rm AA}$.

The observed shift in the peak of $R_{\rm AA}(p_T)$ with $\Delta\phi$ illustrates an important property of collective motion of the medium. The collective motion does not simply superimpose azimuthal variation on the particles produced at a given p_T; rather, it provides a $\Delta\phi$-dependent shift and/or broadening in the transverse momentum spectrum of the produced particles. The resulting distortion will be the smallest for particles produced at angles normal to the reaction plane and will be largest for particles produced in the plane. Any collective shift of soft particles to higher p_T will increase the measured $R_{\rm AA}(\Delta\phi, p_T)$ for small $\Delta\phi$ relative to large $\Delta\phi$ values producing a simultaneous increase in both the $\Delta\phi$-integrated $R_{\rm AA}$

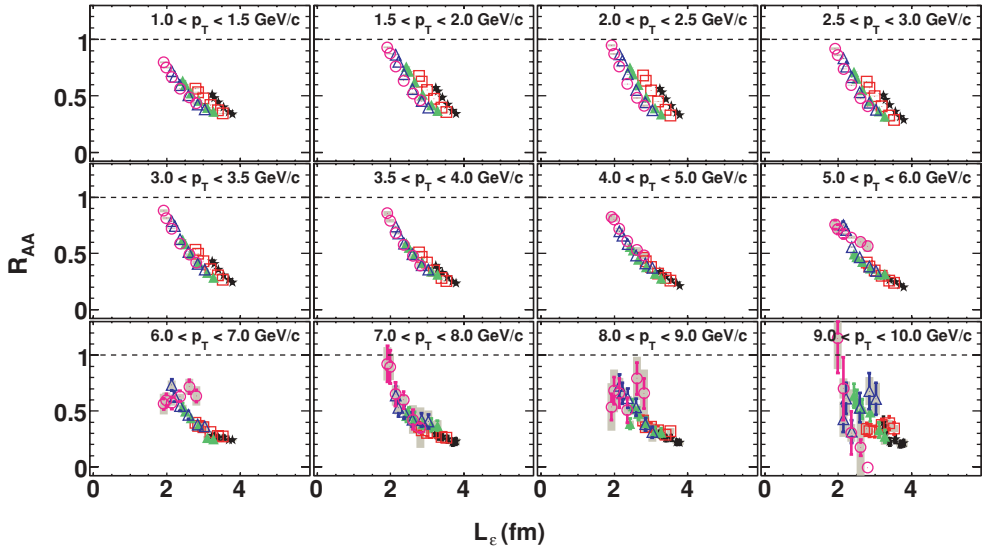

FIG. 22. (Color online) π^0 $R_{\rm AA}$ versus L_ϵ based on the rms radius. Colors/data points as in Fig. 21.

and the v_2. With increasing p_T, an expected decrease in the soft contamination would naturally explain the simultaneous reduction in v_2 and $\Delta\phi$-integrated $R_{\rm AA}$ evident in the 10–20% and 20–30% bins where the separation between the $R_{\rm AA}(p_T)$ curves for different $\Delta\phi$ bins decreases while the average $R_{\rm AA}$ also decreases. We will return to investigate this correlation again below.

The 40–50% and 50–60% centrality bins in Fig. 15 show little of the peaking near 2 GeV/c, especially in $\Delta\phi$ bins not aligned with the reaction plane. Nonetheless the v_2 values for the more peripheral bins reach the same large maximum values, $v_2 \sim 0.2$, at intermediate p_T as the v_2 values for more central bins where the peak in $R_{\rm AA}(p_T)$ is more prominent. Thus, while the peaking in $R_{\rm AA}(p_T)$ is less prominent in the more peripheral bins, the relative difference between the in-plane and out-of-plane π^0 yields in the 40–50% centrality bin is comparable to that in the 20–30% centrality bin. However, it is possible that the large $\Delta\phi$ dependence in the more peripheral bins and the apparent persistence of that variation to high p_T in the 40–50% centrality bin more directly reflect the larger spatial anisotropy of the collision zone in more peripheral collisions. The question of whether the π^0 suppression measurements presented here can be understood on the basis of geometry and jet quenching will be more fully explored in the following section.

We have observed above that the p_T and centrality dependence of $R_{\rm AA}$ indicate a correlation between inclusive $R_{\rm AA}$ and v_2 such that the out-of-plane π^0 yields vary only slowly with p_T or centrality while the in-plane yields approach the out-of-plane yields with increasing p_T or increasing $N_{\rm part}$. The correlation between inclusive $R_{\rm AA}$ and v_2 may indicate that the yields or $R_{\rm AA}$ of π^0's measured in plane and out of plane more directly reflect the underlying physics responsible for the azimuthal variation than the $\Delta\phi$-integrated yield or $R_{\rm AA}$ and the amplitude of the $\Delta\phi$ modulation, v_2. Indeed, we have argued above that at higher p_T the centrality dependence of $R_{\rm AA}(\Delta\phi)$ may reflect the geometry of jet quenching. At intermediate p_T, the $R_{\rm AA}(p_T)$ results suggest contamination of the in-plane yields by soft production and a simultaneous decrease in $R_{\rm AA}$ and v_2 with increasing p_T as the relative contribution of collective soft processes to π^0 production decreases. To more directly demonstrate the correlation that forms the basis of these arguments we show in Fig. 20 a plot of v_2 versus the inclusive $R_{\rm AA}$ for centralities from 0 to 60%. Data are displayed for $p_T > 2$ GeV/c. The intermediate centrality bins show a correlated increase of v_2 and $R_{\rm AA}$ consistent with the discussion above and a possible saturation of v_2 for larger $R_{\rm AA}$ values. In fact, the trends for different centrality bins appear to be in general agreement. However, their exact relationship and establishing or excluding a causal connection require further investigation.

C. Nuclear modification factor dependence on path length

The centrality of a collision fixes the geometry of the overlap region between the nuclei, and fixing the angle of emission of the particles further constrains the average path length through the medium. We can use this feature to study the dependence of the nuclear modification factor on the path length traversed by the partons. We investigate the path length dependence by expanding on several methods previously described in Ref. [34]. We start with three estimators of the path length that are purely geometric, and one that includes the color density of the medium in its calculation:

(i) We start by modeling the overlap region as an ellipse defined by

$$\frac{x^2}{b^2} + \frac{y^2}{a^2} = 1, \tag{14}$$

where the minor axis b is oriented in the x direction and is parallel to the reaction plane. The axes a and b are fixed by the intersection in the transverse plane of two hard spheres with $R = 6.8$ fm. In terms of the spatial eccentricity $\epsilon = \langle y^2 - x^2\rangle/\langle y^2 + x^2\rangle$ (often used with

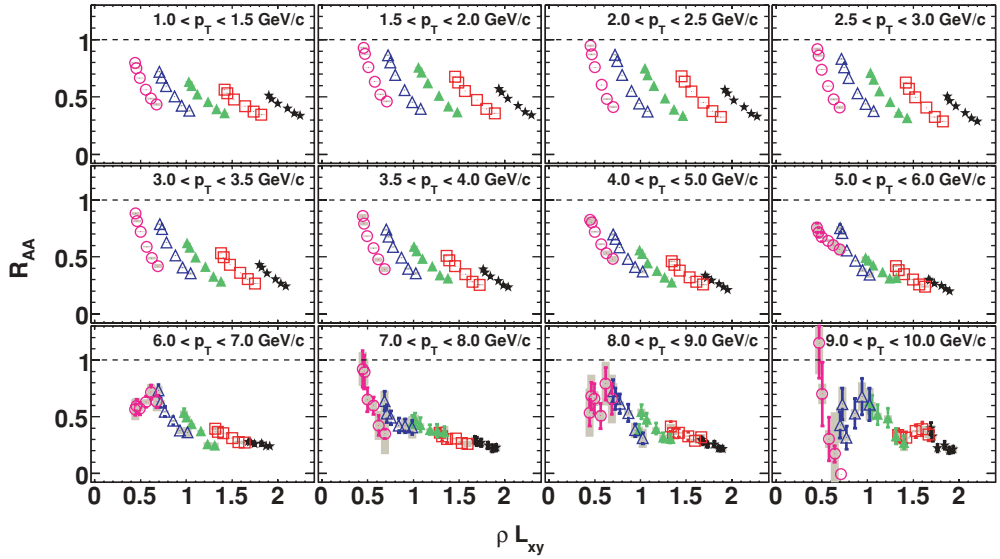

FIG. 23. (Color online) π^0 $R_{\rm AA}$ versus ρL_{xy}. The units of ρL_{xy} are participant × fm. Colors/data points as in Fig. 21.

Glauber calculations), we can express the distance from the origin to the edge of the ellipse at a given angle:

$$L_\epsilon(\Delta\phi) = \frac{b\sqrt{1+\epsilon}}{\sqrt{1+\epsilon\cos 2\Delta\phi}}. \tag{15}$$

Because this length starts at the origin, and does not take into account color density, the expression provides a very simple estimator with which we can evaluate the dependence of the $R_{\rm AA}$ on path length. We will refer to the hard sphere result as $L_{\epsilon,hs}$.

(ii) Instead of an ellipse strictly defined by the transverse profile of two hard spheres, we model the collision region as an effective ellipse whose dimensions are determined by equating the rms radius and eccentricity to the corresponding quantities calculated from the transverse distribution of participant density based on standard Glauber calculations. This length, L_ϵ, is evaluated using the same expression as Eq. (15), with $b = \sqrt{x^2}$. Both quantities are determined using the PHENIX Glauber model [48].

(iii) For a more realistic approach, we evaluate the distance along the parton's path weighted by the participant density,

$$\rho L_{xy} = \int_0^\infty dl \rho_{\rm part}(x_0 + l\cos\Delta\phi, y_0 + l\sin\Delta\phi), \tag{16}$$

where (x_0, y_0) is the hard-scattering position and $\Delta\phi$ is the angle of the jet with respect to the x axis. The jet production point is sampled from a Monte Carlo using a weighted $T_{\rm AA}(x, y)$ distribution and a uniform $\Delta\phi$ distribution. The participant density, assumed to be proportional to the color density, is calculated from the Glauber model. The $\rho_{\rm part}$ density in Eq. (16) is modeled using a 1D Bjorken expansion,

$$\rho_c(\tau) \propto \left(\frac{\tau^2/\tau_0^2}{1+\tau^2/\tau_0^2}\right)\left(\frac{\tau_0}{\tau}\right).$$

Thus ρL_{xy} roughly represents LPM energy loss [51]. Note that ρ_c approaches the same $1/\tau$ dependence as the standard $\rho \propto \tau_0/\tau$ but differs from by a factor of 2 at $\tau = \tau_0$ (additionally this form is regular at $\tau = 0$).

(iv) Finally, we modify ρL_{xy} by normalizing it by the value of the participant density at the center of the collision region, $\rho_{\rm cent} = \rho_{\rm part}(0, 0)$. As a result, $\rho L_{xy}/\rho_{\rm cent}$ is an estimator based on geometry alone but also accounts for the effect of the density distribution both on the jet production point as well as the path from that point to the edge of the medium.

Figures 21–24 show the $R_{\rm AA}$ dependence on $L_{\epsilon,hs}$, L_ϵ, ρL_{xy}, and $\rho L_{xy}/\rho_{\rm cent}$, respectively. The results shown in this article cover the p_T range p_T = 1–10 GeV/c, not only extending the measurement presented previously but allowing a much finer binning in p_T. The statistical errors in the $R_{\rm AA}$ measurements are represented by error bars (see Sec. IV B). The systematic errors shown in these data are on the $R_{\rm AA}$ values only and are indicated by the filled boxes. The major contribution to the systematic error in the L_ϵ values is the determination of $N_{\rm part}$ and is at the 10–20% level.

Both the $L_{\epsilon,hs}$ and L_ϵ behavior show an interesting degree of scaling. This result is all the more unexpected because of the overly simple geometric picture they represent. Despite the simplistic picture they present, they both exhibit striking universality: the hard sphere $R_{\rm AA}(L_{\epsilon,hs})$ scales well in the low-p_T region (as high as $p_T \approx 4$ GeV/c) while $R_{\rm AA}(L_\epsilon)$ scales well to higher p_T, at least one bin in p_T beyond $L_{\epsilon,hs}$ (though one might argue qualitatively this trend continues even higher when the most peripheral centrality is excluded). The more precise p_T dependence available in this data set reveals a slight

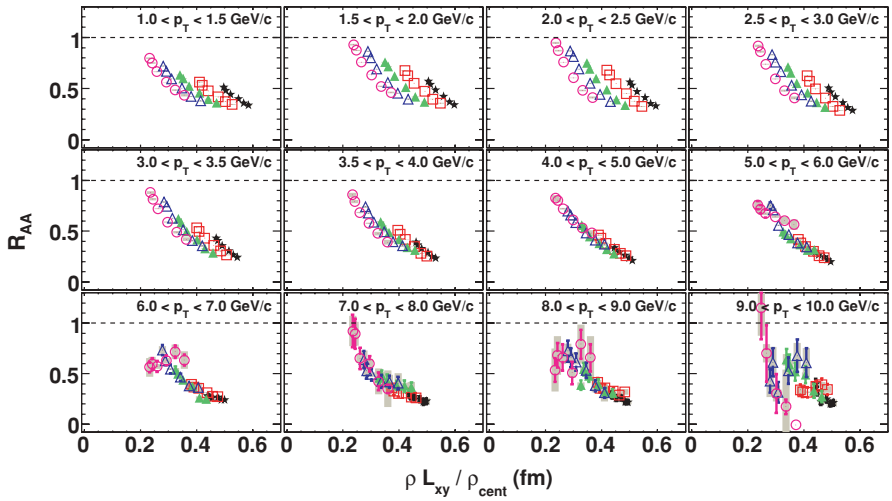

FIG. 24. (Color online) π^0 $R_{\rm AA}$ versus $\rho L_{xy}/\rho_{\rm cent}$. The units of $\rho L_{xy}/\rho_{\rm cent}$ are fm. Colors/data points as in Fig. 21.

deviation from the universality with L_ϵ that was previously reported [34].

By contrast, we expect the ρL_{xy} estimator to provide a somewhat more intuitive and concrete picture, as it represents a more realistic approach to the geometry and medium. Because we expect radiative energy loss to play a greater role at high p_T, this should be the estimator that would provide the best scaling. In fact, at the higher-p_T range, a universality does emerge, though not until $p_T \approx 6$ GeV/c. Below that value, the measured $R_{\rm AA}$ points lie on parallel, but separate, curves. When ρL_{xy} is normalized to the central density, data again exhibit a more universal dependence over a wider p_T range than what is seen with ρL_{xy} alone, as shown in Fig. 24.

When considered together these results offer a rich picture. At low to moderate p_T simple geometry may play a larger role in determining the final level of $R_{\rm AA}$ than conventionally thought. At higher p_T the scaling motivated by energy loss (ρL_{xy}) describes the data well. We note that there are three possible (and not necessarily exclusive) interpretations: (i) at low to moderate p_T the combined effects of the boost due to expansion and fragmentation are sensitive primarily to the difference in lengths traveled by the partons, and only weakly dependent on other parameters; (ii) we need to restrict the analysis of the $\pi^0 R_{\rm AA}$ to $p_T > 5$ GeV/c to be in the range where fragmentation followed by energy loss dominates; or (iii) the assumption that energy loss does not depend linearly on color density is correct [33] and leads to a departure from scaling with ρL_{xy} at low to moderate p_T.

V. SUMMARY AND CONCLUSIONS

We have presented measurements for the azimuthal anisotropy of neutral pions in Au + Au collisions at $\sqrt{s_{NN}} =$ 200 GeV. These measurements include the v_2 and $R_{\rm AA}(\Delta\phi)$ of π^0s as a function of transverse momentum and centrality. The v_2 has been measured from $p_T \approx 1$–10 GeV/c in eight centrality bins and four combined centrality bins. The $R_{\rm AA}$ has been measured in the same p_T range in six centrality bins. In addition, the $R_{\rm AA}$ dependence on effective path length through the collision region has been presented for five centralities.

The general trend seen in the $v_2(p_T)$ data is an initial increase in v_2 with increasing p_T, peaking of the v_2 in the region of $2 < p_T < 3$ GeV/c, followed by a decrease in the v_2. We have argued that such a trend implies a transition from particle production dominated by soft processes to a p_T region dominated by hard processes. To quantify the p_T and centrality evolution of v_2, we have fit its p_T dependence to an empirical expression that allows for such a transition. While the statistical precision of the high-p_T data limits the conclusions we can draw from the fits, it is clear that the data support the assumption of a decreased dominance of soft processes transitioning to an increased dominance of hard process with increasing p_T. The more peripheral bins suggest that a p_T-independent v_2 may be reached by $p_T \sim 5$ GeV/c.

The differential probes represented by $R_{\rm AA}(\Delta\phi)$ provide a more sophisticated handle on the role of geometry in the collision region. For example, we see that in midcentrality collisions the suppression of pions out of plane is approximately the same as the suppression in more central collisions. The data suggest that the interplay between the two main effects, namely collective flow and jet quenching, may take place not only along the expected transition in p_T from soft to hard physics but perhaps also azimuthally, with the quenching effects being dominant along the direction normal to the reaction plane. To further shed light on the transition from soft to hard p_T regions, we have fit the maxima of midcentral $R_{\rm AA}(p_T)$ in each $\Delta\phi$ range. Between the in-plane and out-of-plane directions, we observe a shift of 0.4 GeV/c in position of the peak of the spectrum.

To further clarify the centrality evolution of the azimuthal dependence of the π^0 suppression, we have presented the $R_{\rm AA}$ as a function of $N_{\rm part}$ in fixed p_T bins, for three directions: along the reaction plane, normal to the reaction plane, and

midway between. For $N_{\rm part} \gtrsim 100$, the $R_{\rm AA}$ along the normal to the reaction plane is almost constant, a trend seen in most p_T bins. By contrast, the $R_{\rm AA}$ nearest to the reaction plane drops by almost a factor of two, converging on the out-of-plane value at the highest $N_{\rm part}$. This important feature may provide the most compelling argument for geometry as the source of suppression. Because the path length in the direction normal to the reaction plane varies slowly with centrality, we would expect the $R_{\rm AA}$ to be nearly flat. Conversely, the in-plane path length will be sensitive to the degree of overlap and strongly influence the observed $R_{\rm AA}$. Thus it would lead to a small suppression in peripheral collisions while eventually converging on the same value as seen normal to the plane as the anisotropy vanishes in more central collisions. This effect is further borne out in the correlation observed between v_2 and the inclusive $R_{\rm AA}$. However, we have also argued that contamination from soft production could produce a similar behavior and we have no independent indication of how far in p_T soft contamination might extend. Nonetheless, under both interpretations we can conclude that the $R_{\rm AA}$ for pions produced along the normal to the reaction plane more directly reflects the physics of quenching. We also conclude that the correlation between $R_{\rm AA}$ and v_2 makes separate treatment of these quantities disadvantageous.

We have examined $R_{\rm AA}$ as function of the average path length of the parent parton through the overlap region in the collision, through the estimators $L_{\epsilon,hs}$, L_ϵ, $\rho L_{xy}/\rho_{\rm cent}$, and ρL_{xy}. Each of the first three quantities represents a progressively more sophisticated estimator for the distance traveled by the parton, with ρL_{xy} at the end providing a proxy for LPM energy loss. Comparison of the scaling with these three measures of lengths seems to suggest that the pion suppression at low to moderate p_T is mostly dependent on the simple geometric length. The estimator that should in principle be the most realistic one, ρL_{xy}, exhibits good universality at the highest p_T values, suggesting that energy-loss comparisons should be restricted to the p_T range $p_T > 5$ GeV/c. The importance of simple geometry at low to moderate p_T is further supported when ρL_{xy} is normalized by the participant density at the center. This normalization effectively makes ρL_{xy} a length. These geometric descriptions offer a description of the suppression both at low- and high-p_T regions, clearly showing a transition between the ranges. The features seen in the $R_{\rm AA}$ as function of path length tie in consistently with the observations of a transition in the behavior of the measured v_2. These two observables, v_2 and $R_{\rm AA}(\Delta\phi)$, analyzed together provide a valuable set of probes for understanding the processes governing the suppression of yields in Au + Au collisions.

ACKNOWLEDGMENTS

We thank the staff of the Collider-Accelerator and Physics Departments at Brookhaven National Laboratory and the staff of the other PHENIX participating institutions for their vital contributions. We acknowledge support from the Office of Nuclear Physics in the Office of Science of the Department of Energy, the National Science Foundation, Abilene Christian University Research Council, Research Foundation of SUNY, and Dean of the College of Arts and Sciences, Vanderbilt University (USA), Ministry of Education, Culture, Sports, Science, and Technology and the Japan Society for the Promotion of Science (Japan), Conselho Nacional de Desenvolvimento Científico e Tecnológico and Fundação de Amparo à Pesquisa do Estado de São Paulo (Brazil), Natural Science Foundation of China (People's Republic of China), Centre National de la Recherche Scientifique, Commissariat à l'Énergie Atomique, and Institut National de Physique Nucléaire et de Physique des Particules (France), Ministry of Industry, Science and Tekhnologies, Bundesministerium für Bildung und Forschung, Deutscher Akademischer Austausch Dienst, and Alexander von Humboldt Stiftung (Germany), Hungarian National Science Fund, OTKA (Hungary), Department of Atomic Energy (India), Israel Science Foundation (Israel), Korea Research Foundation and Korea Science and Engineering Foundation (Korea), Ministry of Education and Science, Russia Academy of Sciences, Federal Agency of Atomic Energy (Russia), VR and the Wallenberg Foundation (Sweden), the US Civilian Research and Development Foundation for the Independent States of the Former Soviet Union, the US-Hungarian NSF-OTKA-MTA, and the US-Israel Binational Science Foundation.

APPENDIX A: DATA TABLES

TABLE I. π^0 v_2 for 0–5% and 5–10% centrality. All errors are absolute.

Centrality	$\langle p_{\rm T}\rangle$ GeV/c	v_2	Stat. error		Syst. error
	1.21	0.052	+0.034	−0.034	0.011
	1.70	0.035	+0.022	−0.022	0.007
	2.20	0.051	+0.020	−0.020	0.010
	2.70	0.076	+0.023	−0.023	0.016
	3.21	0.039	+0.029	−0.029	0.008
	3.71	0.059	+0.039	−0.039	0.012
0–5%	4.37	0.040	+0.042	−0.042	0.008
	5.40	0.040	+0.070	−0.070	0.008
	6.41	0.052	+0.115	−0.115	0.011
	7.43	0.160	+0.206	−0.206	0.033
	8.43	0.168	+0.146	−0.146	0.034
	9.44	0.132	+0.171	−0.171	0.027
	1.21	0.079	+0.020	−0.020	0.010
	1.71	0.083	+0.013	−0.013	0.010
	2.20	0.106	+0.012	−0.012	0.013
	2.70	0.100	+0.014	−0.014	0.012
	3.21	0.109	+0.018	−0.018	0.014
	3.71	0.075	+0.024	−0.024	0.009
5–10%	4.38	0.091	+0.026	−0.026	0.011
	5.40	0.064	+0.041	−0.041	0.008
	6.41	0.062	+0.077	−0.077	0.008
	7.42	0.054	+0.158	−0.158	0.007
	8.43	0.002	+0.097	−0.097	0.0002
	9.44	0.118	+0.136	−0.136	0.015

TABLE II. π^0 v_2 for other centralities. All errors are absolute.

Centrality	$\langle p_T \rangle$ GeV/c	v_2	Stat. error		Syst. error
	1.20	0.066	+0.018	−0.018	0.012
	1.71	0.061	+0.012	−0.012	0.011
	2.20	0.078	+0.011	−0.011	0.014
	2.70	0.087	+0.013	−0.013	0.016
	3.21	0.079	+0.016	−0.016	0.014
	3.71	0.070	+0.021	−0.021	0.013
0–10%	4.37	0.067	+0.023	−0.023	0.012
	5.40	0.054	+0.037	−0.037	0.010
	6.41	0.066	+0.064	−0.064	0.012
	7.42	0.112	+0.124	−0.124	0.020
	8.43	0.071	+0.087	−0.087	0.013
	9.44	0.189	+0.108	−0.108	0.034
	1.20	0.106	+0.010	−0.010	0.008
	1.71	0.131	+0.006	−0.006	0.010
	2.20	0.138	+0.006	−0.006	0.010
	2.70	0.141	+0.007	−0.007	0.010
	3.21	0.145	+0.009	−0.009	0.011
	3.71	0.130	+0.012	−0.012	0.010
10–20%	4.37	0.114	+0.014	−0.014	0.008
	5.40	0.105	+0.024	−0.024	0.008
	6.41	0.043	+0.037	−0.037	0.003
	7.42	0.075	+0.088	−0.088	0.006
	8.43	0.076	+0.059	−0.059	0.006
	9.44	0.151	+0.083	−0.083	0.011
	1.21	0.125	+0.008	−0.008	0.008
	1.71	0.159	+0.005	−0.005	0.010
	2.20	0.183	+0.005	−0.005	0.011
	2.70	0.193	+0.006	−0.006	0.012
	3.21	0.172	+0.008	−0.008	0.010
	3.71	0.175	+0.011	−0.011	0.010
20–30%	4.38	0.147	+0.012	−0.012	0.009
	5.40	0.139	+0.022	−0.022	0.008
	6.41	0.097	+0.037	−0.037	0.006
	7.42	0.074	+0.073	−0.073	0.004
	8.43	0.070	+0.059	−0.059	0.004
	9.44	−0.035	+0.087	−0.087	0.002
	1.21	0.143	+0.007	−0.007	0.008
	1.71	0.181	+0.005	−0.005	0.010
	2.20	0.196	+0.005	−0.005	0.011
	2.71	0.199	+0.007	−0.007	0.011
	3.21	0.194	+0.009	−0.009	0.011
	3.71	0.163	+0.012	−0.012	0.009
30–40%	4.38	0.172	+0.013	−0.013	0.010
	5.40	0.121	+0.024	−0.024	0.007
	6.41	0.200	+0.042	−0.042	0.011
	7.43	0.070	+0.088	−0.088	0.004
	8.43	0.113	+0.071	−0.071	0.006
	9.44	0.199	+0.118	−0.118	0.011
	1.20	0.160	+0.008	−0.008	0.009
	1.71	0.193	+0.006	−0.006	0.010
	2.21	0.208	+0.006	−0.006	0.011
	2.71	0.194	+0.008	−0.008	0.010
	3.21	0.200	+0.011	−0.011	0.011
	3.72	0.182	+0.015	−0.015	0.010

TABLE II. *(Continued.)*

Centrality	$\langle p_T \rangle$ GeV/c	v_2	Stat. error		Syst. error
40–50%	4.38	0.161	+0.018	−0.018	0.009
	5.40	0.198	+0.032	−0.032	0.011
	6.41	0.175	+0.055	−0.055	0.009
	7.42	0.106	+0.133	−0.133	0.006
	8.43	0.196	+0.112	−0.112	0.011
	9.44	−0.084	+0.214	−0.214	0.005
	1.21	0.153	+0.010	−0.010	0.009
	1.71	0.175	+0.008	−0.008	0.010
	2.21	0.204	+0.009	−0.009	0.012
	2.71	0.200	+0.012	−0.012	0.012
	3.21	0.181	+0.016	−0.016	0.011
	3.72	0.187	+0.023	−0.023	0.011
50–60%	4.38	0.141	+0.028	−0.028	0.008
	5.40	0.070	+0.050	−0.050	0.004
	6.41	−0.044	+0.097	−0.097	0.003
	7.42	0.235	+0.168	−0.168	0.014
	8.43	−0.042	+0.234	−0.234	0.002
	9.44	0.520	+0.428	−0.428	0.031
	1.20	0.083	+0.011	−0.011	0.011
	1.71	0.091	+0.007	−0.007	0.012
	2.20	0.104	+0.007	−0.007	0.014
	2.70	0.110	+0.008	−0.008	0.015
	3.21	0.107	+0.010	−0.010	0.015
	3.71	0.097	+0.013	−0.013	0.013
0–20%	4.37	0.088	+0.014	−0.014	0.012
	5.40	0.077	+0.023	−0.023	0.010
	6.41	0.056	+0.039	−0.039	0.007
	7.42	0.096	+0.081	−0.079	0.013
	8.43	0.074	+0.055	−0.054	0.010
	9.44	0.170	+0.074	−0.072	0.023
	1.21	0.133	+0.005	−0.005	0.008
	1.71	0.169	+0.004	−0.004	0.010
	2.20	0.189	+0.004	−0.004	0.011
	2.71	0.197	+0.005	−0.005	0.012
	3.21	0.182	+0.006	−0.006	0.011
	3.71	0.171	+0.008	−0.008	0.010
20–40%	4.38	0.158	+0.009	−0.009	0.009
	5.40	0.132	+0.016	−0.016	0.008
	6.41	0.140	+0.027	−0.027	0.008
	7.42	0.071	+0.055	−0.054	0.004
	8.43	0.088	+0.045	−0.044	0.005
	9.44	0.062	+0.070	−0.069	0.004
	1.21	0.159	+0.007	−0.007	0.009
	1.71	0.188	+0.005	−0.005	0.010
	2.21	0.208	+0.006	−0.006	0.012
	2.71	0.198	+0.008	−0.008	0.011
	3.21	0.195	+0.010	−0.010	0.011
	3.72	0.185	+0.014	−0.014	0.010
40–60%	4.38	0.155	+0.017	−0.017	0.009
	5.40	0.149	+0.031	−0.030	0.008
	6.41	0.093	+0.056	−0.055	0.005
	7.42	0.152	+0.118	−0.113	0.008
	8.43	0.114	+0.126	−0.124	0.006
	9.44	0.168	+0.266	−0.231	0.009

TABLE II. *(Continued.)*

Centrality	$\langle p_T \rangle$ GeV/c	v_2	Stat. error		Syst. error
	1.20	0.106	+0.009	−0.009	0.013
	1.71	0.125	+0.006	−0.006	0.015
	2.20	0.142	+0.006	−0.006	0.017
	2.71	0.146	+0.008	−0.008	0.018
	3.21	0.143	+0.011	−0.011	0.017
	3.71	0.136	+0.015	−0.015	0.016
0–92%	4.38	0.127	+0.017	−0.017	0.015
	5.40	0.108	+0.033	−0.033	0.013
	6.41	0.084	+0.059	−0.059	0.010
	7.42	0.083	+0.136	−0.145	0.009
	8.43	0.113	+0.099	−0.109	0.011
	9.44	0.149	+0.156	−0.123	0.012

TABLE III. R_{AA} vs. path length for (upper) $1.0 < p_T < 1.5$ and (lower) $1.5 < p_T < 2.0$ GeV/c.

Centrality	$\Delta\phi$	L_ϵ	ρL_{xy}	R_{AA}	Stat. error (abs.)	Sys. error (abs.)
	0–15	3.23	1.90	0.514	0.009	0.005
	15–30	3.29	1.93	0.481	0.009	0.003
	30–45	3.41	2.00	0.443	0.008	0.001
10–20%	45–60	3.55	2.11	0.400	0.007	0.001
	60–75	3.69	2.18	0.358	0.007	0.004
	75–90	3.78	2.24	0.337	0.006	0.006
	0–15	2.78	1.42	0.565	0.009	0.004
	15–30	2.85	1.45	0.533	0.008	0.003
	30–45	2.99	1.52	0.477	0.008	0.001
20–30%	45–60	3.19	1.64	0.421	0.007	0.001
	60–75	3.39	1.74	0.371	0.006	0.003
	75–90	3.52	1.82	0.346	0.006	0.005
	0–15	2.43	1.03	0.634	0.009	0.004
	15–30	2.50	1.06	0.599	0.009	0.003
	30–45	2.66	1.12	0.526	0.008	0.001
30–40%	45–60	2.87	1.24	0.459	0.007	0.001
	60–75	3.11	1.33	0.397	0.006	0.004
	75–90	3.27	1.42	0.360	0.005	0.005
	0–15	2.14	0.70	0.721	0.009	0.005
	15–30	2.21	0.73	0.669	0.009	0.004
	30–45	2.37	0.78	0.596	0.008	0.002
40–50%	45–60	2.59	0.87	0.505	0.007	0.002
	60–75	2.84	0.95	0.424	0.006	0.005
	75–90	3.03	1.03	0.379	0.005	0.007
	0–15	1.92	0.44	0.798	0.010	0.009
	15–30	1.99	0.46	0.751	0.010	0.007
	30–45	2.14	0.49	0.665	0.008	0.002
50–60%	45–60	2.36	0.56	0.562	0.007	0.003
	60–75	2.61	0.61	0.485	0.006	0.007
	75–90	2.81	0.68	0.435	0.006	0.010
	0–15	3.23	1.94	0.570	0.007	0.003
	15–30	3.29	1.96	0.539	0.007	0.002
	30–45	3.41	2.03	0.486	0.006	0.001
10–20%	45–60	3.55	2.15	0.424	0.009	0.001

TABLE III. *(Continued.)*

Centrality	$\Delta\phi$	L_ϵ	ρL_{xy}	R_{AA}	Stat. error (abs.)	Sys. error (abs.)
	60–75	3.69	2.22	0.370	0.005	0.003
	75–90	3.78	2.29	0.341	0.005	0.004
	0–15	2.78	1.46	0.677	0.008	0.003
	15–30	2.85	1.49	0.626	0.008	0.002
	30–45	2.99	1.57	0.552	0.007	0.001
20–30%	45–60	3.19	1.70	0.475	0.006	0.001
	60–75	3.39	1.80	0.397	0.005	0.002
	75–90	3.52	1.89	0.358	0.004	0.003
	0–15	2.43	1.06	0.758	0.009	0.003
	15–30	2.50	1.09	0.716	0.008	0.002
	30–45	2.66	1.16	0.622	0.007	0.001
30–40%	45–60	2.87	1.28	0.512	0.006	0.001
	60–75	3.11	1.38	0.420	0.005	0.003
	75–90	3.27	1.48	0.370	0.004	0.004
	0–15	2.14	0.72	0.865	0.010	0.004
	15–30	2.21	0.75	0.802	0.009	0.003
	30–45	2.37	0.80	0.691	0.008	0.001
40–50%	45–60	2.59	0.90	0.561	0.006	0.001
	60–75	2.84	0.99	0.455	0.005	0.004
	75–90	3.03	1.08	0.398	0.005	0.006
	0–15	1.92	0.45	0.929	0.010	0.008
	15−30	1.99	0.47	0.874	0.010	0.006
	30–45	2.14	0.51	0.757	0.009	0.002
50–60%	45−60	2.36	0.58	0.635	0.007	0.002
	60–75	2.61	0.64	0.523	0.006	0.007
	75−90	2.81	0.71	0.462	0.005	0.009

TABLE IV. R_{AA} vs. path length for (upper) $2.0 < p_T < 2.5$ and (lower) $2.5 < p_T < 3.0$ GeV/c.

Centrality	$\Delta\phi$	L_ϵ	ρL_{xy}	R_{AA}	Stat. error (abs.)	Sys. error (abs.)
	0–15	3.23	1.92	0.562	0.007	0.003
	15–30	3.29	1.95	0.534	0.007	0.002
	30–45	3.41	2.02	0.470	0.006	0.001
10–20%	45–60	3.55	2.13	0.413	0.006	0.001
	60–75	3.69	2.21	0.354	0.005	0.003
	75–90	3.78	2.28	0.329	0.004	0.004
	0–15	2.78	1.45	0.681	0.008	0.003
	15–30	2.85	1.48	0.633	0.008	0.002
	30–45	2.99	1.56	0.547	0.007	0.001
20–30%	45–60	3.19	1.69	0.452	0.006	0.001
	60–75	3.39	1.79	0.375	0.005	0.003
	75–90	3.52	1.88	0.325	0.004	0.004
	0–15	2.43	1.05	0.752	0.009	0.003
	15–30	2.50	1.08	0.691	0.008	0.002
	30–45	2.66	1.15	0.597	0.007	0.001
30–40%	45–60	2.87	1.27	0.490	0.006	0.001
	60–75	3.11	1.37	0.392	0.005	0.003
	75–90	3.27	1.46	0.339	0.004	0.004

TABLE IV. *(Continued.)*

Centrality	$\Delta\phi$	L_ϵ	ρL_{xy}	R_{AA}	Stat. error (abs.)	Sys. error (abs.)
	0–15	2.14	0.72	0.869	0.010	0.005
	15–30	2.21	0.75	0.813	0.009	0.004
	30–45	2.37	0.80	0.691	0.008	0.001
40–50%	45–60	2.59	0.90	0.550	0.006	0.001
	60–75	2.84	0.99	0.443	0.005	0.004
	75–90	3.03	1.08	0.375	0.004	0.006
	0–15	1.92	0.45	0.946	0.011	0.009
	15–30	1.99	0.47	0.870	0.010	0.007
	30–45	2.14	0.50	0.757	0.009	0.003
50–60%	45–60	2.36	0.57	0.606	0.007	0.003
	60–75	2.61	0.63	0.482	0.006	0.007
	75–90	2.81	0.70	0.413	0.005	0.010
	0–15	3.23	1.87	0.504	0.007	0.003
	15–30	3.29	1.90	0.467	0.007	0.002
	30–45	3.41	1.96	0.421	0.006	0.001
10–20%	45–60	3.55	2.07	0.360	0.005	0.001
	60–75	3.69	2.14	0.315	0.005	0.003
	75–90	3.78	2.20	0.288	0.004	0.004
	0–15	2.78	1.42	0.626	0.009	0.003
	15–30	2.85	1.45	0.573	0.008	0.002
	30–45	2.99	1.52	0.499	0.007	0.001
20–30%	45–60	3.19	1.64	0.409	0.006	0.001
	60–75	3.39	1.74	0.326	0.005	0.003
	75–90	3.52	1.82	0.287	0.004	0.004
	0–15	2.43	1.03	0.713	0.009	0.004
	15–30	2.50	1.07	0.654	0.009	0.003
	30–45	2.66	1.13	0.550	0.007	0.001
30–40%	45–60	2.87	1.25	0.459	0.006	0.001
	60–75	3.11	1.34	0.364	0.005	0.003
	75–90	3.27	1.43	0.318	0.004	0.005
	0–15	2.14	0.72	0.832	0.011	0.006
	15–30	2.21	0.74	0.758	0.010	0.004
	30–45	2.37	0.79	0.665	0.009	0.002
40–50%	45–60	2.59	0.89	0.534	0.007	0.002
	60–75	2.84	0.98	0.439	0.006	0.005
	75–90	3.03	1.07	0.376	0.005	0.007
	0–15	1.92	0.45	0.916	0.012	0.011
	15–30	1.99	0.47	0.861	0.011	0.008
	30–45	2.14	0.50	0.738	0.010	0.003
50–60%	45–60	2.36	0.57	0.594	0.008	0.003
	60–75	2.61	0.63	0.480	0.006	0.010
	75–90	2.81	0.70	0.409	0.006	0.013

TABLE V. R_{AA} vs. path length for (upper) $3.0 < p_T < 3.5$ and (lower) $3.5 < p_T < 4.0$ GeV/c.

Centrality	$\Delta\phi$	L_ϵ	ρL_{xy}	R_{AA}	Stat. error (abs.)	Sys. error (abs.)
	0–15	3.23	1.80	0.430	0.008	0.003
	15–30	3.29	1.82	0.405	0.007	0.003

TABLE V. *(Continued.)*

Centrality	$\Delta\phi$	L_ϵ	ρL_{xy}	R_{AA}	Stat. error (abs.)	Sys. error (abs.)
	30–45	3.41	1.88	0.355	0.006	0.001
10–20%	45–60	3.55	1.97	0.307	0.006	0.001
	60–75	3.69	2.04	0.266	0.005	0.003
	75–90	3.78	2.09	0.243	0.004	0.004
	0–15	2.78	1.38	0.534	0.009	0.003
	15–30	2.85	1.41	0.497	0.008	0.003
	30–45	2.99	1.48	0.431	0.007	0.001
20–30%	45–60	3.19	1.59	0.360	0.006	0.001
	60–75	3.39	1.67	0.305	0.005	0.003
	75–90	3.52	1.75	0.267	0.005	0.004
	0–15	2.43	1.01	0.622	0.010	0.004
	15–30	2.50	1.04	0.582	0.009	0.003
	30–45	2.66	1.10	0.498	0.008	0.001
30–40%	45–60	2.87	1.21	0.417	0.007	0.001
	60–75	3.11	1.30	0.328	0.005	0.004
	75–90	3.27	1.38	0.285	0.005	0.006
	0–15	2.14	0.71	0.788	0.012	0.007
	15–30	2.21	0.74	0.745	0.012	0.006
	30–45	2.37	0.79	0.625	0.010	0.002
40–50%	45–60	2.59	0.88	0.514	0.008	0.002
	60–75	2.84	0.96	0.407	0.007	0.007
	75–90	3.03	1.05	0.355	0.006	0.009
	0–15	1.92	0.45	0.880	0.015	0.015
	15–30	1.99	0.46	0.814	0.014	0.011
	30–45	2.14	0.50	0.720	0.012	0.004
50–60%	45–60	2.36	0.57	0.589	0.010	0.004
	60–75	2.61	0.63	0.490	0.008	0.013
	75–90	2.81	0.69	0.421	0.007	0.018
	0–15	3.23	1.76	0.390	0.009	0.004
	15–30	3.29	1.78	0.364	0.008	0.003
	30–45	3.41	1.84	0.329	0.007	0.001
10–20%	45–60	3.55	1.93	0.291	0.007	0.001
	60–75	3.69	1.99	0.249	0.006	0.004
	75–90	3.78	2.04	0.234	0.005	0.005
	0–15	2.78	1.36	0.511	0.011	0.004
	15–30	2.85	1.39	0.468	0.010	0.003
	30–45	2.99	1.46	0.418	0.009	0.001
20–30%	45–60	3.19	1.57	0.348	0.007	0.001
	60–75	3.39	1.65	0.281	0.006	0.004
	75–90	3.52	1.72	0.256	0.005	0.006
	0–15	2.43	1.01	0.593	0.012	0.006
	15–30	2.50	1.04	0.552	0.011	0.004
	30–45	2.66	1.10	0.487	0.010	0.002
30–40%	45–60	2.87	1.21	0.418	0.008	0.002
	60–75	3.11	1.29	0.341	0.007	0.005
	75–90	3.27	1.38	0.311	0.007	0.007
	0–15	2.14	0.70	0.738	0.015	0.010
	15–30	2.21	0.73	0.676	0.014	0.007
	30–45	2.37	0.78	0.588	0.012	0.003
40–50%	45–60	2.59	0.87	0.495	0.010	0.003
	60–75	2.84	0.95	0.397	0.008	0.009
	75–90	3.03	1.03	0.356	0.008	0.012

TABLE V. *(Continued.)*

Centrality	$\Delta\phi$	L_ϵ	ρL_{xy}	R_{AA}	Stat. error (abs.)	Sys. error (abs.)
	0–15	1.92	0.44	0.856	0.019	0.021
	15–30	1.99	0.46	0.791	0.017	0.015
	30–45	2.14	0.50	0.682	0.015	0.006
50–60%	45–60	2.36	0.56	0.577	0.013	0.006
	60–75	2.61	0.62	0.477	0.011	0.018
	75–90	2.81	0.68	0.392	0.009	0.023

TABLE VI. R_{AA} vs. path length for (upper) $4.0 < p_T < 5.0$ and (lower) $5.0 < p_T < 6.0$ GeV/c.

Centrality	$\Delta\phi$	L_ϵ	ρL_{xy}	R_{AA}	Stat. error (abs.)	Sys. error (abs.)
	0–15	3.23	1.71	0.336	0.010	0.004
	15–30	3.29	1.73	0.319	0.009	0.003
	30–45	3.41	1.78	0.292	0.009	0.001
10–20%	45–60	3.55	1.86	0.261	0.008	0.001
	60–75	3.69	1.91	0.234	0.007	0.004
	75–90	3.78	1.95	0.213	0.006	0.005
	0–15	2.78	1.34	0.461	0.012	0.004
	15–30	2.85	1.37	0.430	0.012	0.003
	30–45	2.99	1.43	0.381	0.010	0.001
20–30%	45–60	3.19	1.54	0.322	0.009	0.001
	60–75	3.39	1.61	0.284	0.008	0.004
	75–90	3.52	1.68	0.258	0.007	0.006
	0–15	2.43	0.99	0.559	0.015	0.006
	15–30	2.50	1.02	0.527	0.014	0.005
	30–45	2.66	1.08	0.448	0.012	0.002
30–40%	45–60	2.87	1.18	0.379	0.010	0.002
	60–75	3.11	1.26	0.322	0.009	0.006
	75–90	3.27	1.34	0.279	0.008	0.008
	0–15	2.14	0.70	0.697	0.020	0.012
	15–30	2.21	0.72	0.658	0.019	0.009
	30–45	2.37	0.77	0.583	0.016	0.003
40–50%	45–60	2.59	0.87	0.483	0.014	0.004
	60–75	2.84	0.94	0.411	0.012	0.010
	75–90	3.03	1.02	0.372	0.011	0.014
	0–15	1.92	0.45	0.826	0.026	0.026
	15–30	1.99	0.47	0.804	0.025	0.020
	30–45	2.14	0.50	0.722	0.022	0.008
50–60%	45–60	2.36	0.57	0.611	0.019	0.008
	60–75	2.61	0.63	0.534	0.017	0.022
	75–90	2.81	0.70	0.480	0.0155	0.030
	0–15	3.23	1.67	0.301	0.014	0.007
	15–30	3.29	1.68	0.294	0.013	0.005
	30–45	3.41	1.73	0.267	0.012	0.002
10–20%	45–60	3.55	1.81	0.246	0.011	0.002
	60–75	3.69	1.85	0.218	0.010	0.006
	75–90	3.78	1.90	0.199	0.009	0.008
	0–15	2.78	1.31	0.420	0.018	0.008
	15–30	2.85	1.34	0.382	0.017	0.006
	30–45	2.99	1.40	0.347	0.015	0.002

TABLE VI. *(Continued.)*

Centrality	$\Delta\phi$	L_ϵ	ρL_{xy}	R_{AA}	Stat. error (abs.)	Sys. error (abs.)
20–30%	45–60	3.19	1.50	0.301	0.013	0.002
	60–75	3.39	1.56	0.260	0.012	0.007
	75–90	3.52	1.63	0.240	0.011	0.010
	0–15	2.43	0.98	0.492	0.022	0.011
	15–30	2.50	1.01	0.469	0.020	0.008
	30–45	2.66	1.06	0.428	0.019	0.003
30–40%	45–60	2.87	1.17	0.370	0.017	0.003
	60–75	3.11	1.24	0.315	0.015	0.009
	75–90	3.27	1.32	0.318	0.014	0.014
	0–15	2.14	0.70	0.750	0.035	0.021
	15–30	2.21	0.72	0.708	0.032	0.016
	30–45	2.37	0.77	0.557	0.028	0.006
40–50%	45–60	2.59	0.87	0.466	0.023	0.006
	60–75	2.84	0.94	0.385	0.019	0.019
	75–90	3.03	1.02	0.345	0.017	0.027
	0–15	1.92	0.45	0.757	0.039	0.050
	15–30	1.99	0.47	0.715	0.040	0.036
	30–45	2.14	0.50	0.672	0.038	0.013
50–60%	45–60	2.36	0.57	0.642	0.033	0.014
	60–75	2.61	0.63	0.605	0.032	0.038
	75–90	2.81	0.69	0.563	0.030	0.051

TABLE VII. R_{AA} vs. path length for (upper) $6.0 < p_T < 7.0$ and (lower) $7.0 < p_T < 8.0$ GeV/c.

Centrality	$\Delta\phi$	L_ϵ	ρL_{xy}	R_{AA}	Stat. error (abs.)	Sys. error (abs.)
	0–15	3.23	1.68	0.281	0.017	0.011
	15–30	3.29	1.70	0.278	0.017	0.008
	30–45	3.41	1.75	0.261	0.017	0.003
10–20%	45–60	3.55	1.82	0.264	0.018	0.003
	60–75	3.69	1.87	0.241	0.015	0.009
	75–90	3.78	1.91	0.240	0.015	0.012
	0–15	2.78	1.32	0.396	0.026	0.013
	15–30	2.85	1.34	0.368	0.023	0.010
	30–45	2.99	1.40	0.357	0.023	0.004
20–30%	45–60	3.19	1.50	0.312	0.021	0.004
	60–75	3.39	1.57	0.277	0.018	0.011
	75–90	3.52	1.64	0.274	0.017	0.016
	0–15	2.43	0.98	0.537	0.035	0.018
	15–30	2.50	1.00	0.496	0.030	0.013
	30–45	2.66	1.06	0.437	0.029	0.005
30–40%	45–60	2.87	1.16	0.376	0.026	0.006
	60–75	3.11	1.23	0.261	0.018	0.015
	75–90	3.27	1.31	0.249	0.019	0.025
	0–15	2.14	0.70	0.734	0.050	0.038
	15–30	2.21	0.72	0.625	0.043	0.026
	30–45	2.37	0.77	0.546	0.044	0.010
40–50%	45–60	2.59	0.86	0.465	0.036	0.011
	60–75	2.84	0.93	0.377	0.029	0.030
	75–90	3.03	1.01	0.363	0.027	0.046

TABLE VII. *(Continued.)*

Centrality	$\Delta\phi$	L_ϵ	ρL_{xy}	R_{AA}	Stat. error (abs.)	Sys. error (abs.)
	0–15	1.92	0.44	0.564	0.051	0.093
	15−30	1.99	0.46	0.597	0.059	0.070
	30–45	2.14	0.49	0.572	0.054	0.023
50–60%	45–60	2.36	0.56	0.631	0.049	0.024
	60–75	2.61	0.62	0.717	0.063	0.072
	75–90	2.81	0.68	0.635	0.056	0.085
	0–15	3.23	1.67	0.297	0.032	0.026
	15–30	3.29	1.69	0.282	0.037	0.019
	30–45	3.41	1.74	0.272	0.034	0.007
10–20%	45–60	3.55	1.82	0.248	0.030	0.007
	60–75	3.69	1.86	0.222	0.031	0.020
	75–90	3.78	1.91	0.227	0.030	0.030
	0–15	2.78	1.29	0.359	0.037	0.025
	15–30	2.85	1.31	0.327	0.040	0.018
	30–45	2.99	1.37	0.306	0.035	0.007
20–30%	45–60	3.19	1.47	0.308	0.033	0.007
	60–75	3.39	1.53	0.270	0.033	0.020
	75–90	3.52	1.59	0.261	0.029	0.027
	0–15	2.43	0.99	0.458	0.055	0.042
	15–30	2.50	1.02	0.482	0.052	0.033
	30–45	2.66	1.08	0.429	0.063	0.012
30–40%	45–60	2.87	1.18	0.387	0.044	0.012
	60–75	3.11	1.26	0.377	0.057	0.034
	75–90	3.27	1.34	0.369	0.045	0.048
	0–15	2.14	0.69	0.639	0.086	0.091
	15–30	2.21	0.71	0.527	0.079	0.058
	30–45	2.37	0.75	0.492	0.062	0.022
40–50%	45–60	2.59	0.84	0.424	0.066	0.022
	60–75	2.84	0.91	0.420	0.062	0.069
	75–90	3.03	0.99	0.406	0.063	0.099
	0–15	1.92	0.45	0.922	0.161	0.149
	15–30	1.99	0.46	0.895	0.150	0.118
	30–45	2.14	0.50	0.651	0.106	0.039
50–60%	45–60	2.36	0.56	0.598	0.078	0.048
	60–75	2.61	0.62	0.424	0.089	0.128
	75–90	2.81	0.69	0.351	0.042	0.182

TABLE VIII. R_{AA} vs. path length for (upper) $8.0 < p_T < 9.0$ and (lower) $9.0 < p_T < 10.0$ GeV/c.

Centrality	$\Delta\phi$	L_ϵ	ρL_{xy}	R_{AA}	Stat. error (abs.)	Sys. error (abs.)
	0–15	3.23	1.67	0.296	0.030	0.017
	15–30	3.29	1.68	0.280	0.029	0.013
	30–45	3.41	1.73	0.255	0.026	0.005
10–20%	45–60	3.55	1.81	0.258	0.026	0.005
	60–75	3.69	1.86	0.220	0.023	0.013
	75–90	3.78	1.90	0.219	0.022	0.019
	0–15	2.78	1.33	0.415	0.043	0.024
	15–30	2.85	1.36	0.356	0.038	0.016
	30–45	2.99	1.42	0.359	0.038	0.006

TABLE VIII. *(Continued.)*

Centrality	$\Delta\phi$	L_ϵ	ρL_{xy}	R_{AA}	Stat. error (abs.)	Sys. error (abs.)
20–30%	45–60	3.19	1.52	0.329	0.035	0.006
	60–75	3.39	1.59	0.288	0.032	0.017
	75–90	3.52	1.66	0.320	0.033	0.027
	0–15	2.43	0.98	0.387	0.049	0.026
	15–30	2.50	1.01	0.543	0.063	0.029
	30–45	2.66	1.07	0.476	0.056	0.010
30–40%	45–60	2.87	1.17	0.396	0.048	0.010
	60–75	3.11	1.25	0.318	0.041	0.026
	75–90	3.27	1.32	0.308	0.039	0.037
	0–15	2.14	0.70	0.724	0.103	0.072
	15–30	2.21	0.73	0.658	0.094	0.053
	30–45	2.37	0.77	0.614	0.087	0.022
40–50%	45–60	2.59	0.87	0.535	0.076	0.025
	60–75	2.84	0.94	0.382	0.058	0.065
	75–90	3.03	1.03	0.310	0.048	0.086
	0–15	1.92	0.45	0.536	0.118	0.212
	15–30	1.99	0.46	0.682	0.121	0.192
	30–45	2.14	0.50	0.661	0.130	0.065
50–60%	45–60	2.36	0.56	0.508	0.112	0.047
	60–75	2.61	0.62	0.791	0.144	0.193
	75–90	2.81	0.69	0.658	0.135	0.215
	0–15	3.23	1.69	0.397	0.051	0.028
	15–30	3.29	1.71	0.327	0.045	0.018
	30–45	3.41	1.76	0.223	0.034	0.005
10–20%	45–60	3.55	1.84	0.249	0.035	0.007
	60–75	3.69	1.89	0.203	0.030	0.021
	75–90	3.78	1.94	0.213	0.030	0.034
	0–15	2.78	1.33	0.340	0.054	0.038
	15–30	2.85	1.36	0.319	0.051	0.025
	30–45	2.99	1.42	0.316	0.052	0.009
20–30%	45–60	3.19	1.53	0.374	0.058	0.010
	60–75	3.39	1.60	0.392	0.061	0.027
	75–90	3.52	1.67	0.343	0.055	0.032
	0–15	2.43	1.02	0.637	0.108	0.059
	15–30	2.50	1.05	0.588	0.103	0.044
	30–45	2.66	1.11	0.519	0.090	0.018
30–40%	45–60	2.87	1.22	0.491	0.084	0.022
	60–75	3.11	1.31	0.331	0.069	0.054
	75–90	3.27	1.40	0.274	0.057	0.075
	0–15	2.14	0.70	0.428	0.115	0.158
	15–30	2.21	0.72	0.612	0.139	0.155
	30–45	2.37	0.77	0.316	0.102	0.026
40–50%	45–60	2.59	0.86	0.530	0.133	0.039
	60–75	2.84	0.94	0.678	0.162	0.125
	75–90	3.03	1.02	0.609	0.143	0.145
	0–15	1.92	0.45	1.866	0.486	0.498
	15–30	1.99	0.47	1.150	0.310	0.273
	30–45	2.14	0.51	0.702	0.282	0.091
50–60%	45–60	2.36	0.58	0.305	0.192	0.077
	60–75	2.61	0.64	0.172	0.073	0.369
	75–90	2.81	0.71	−0.005	−0.002	−0.812

[1] K. Adcox *et al.* (PHENIX Collaboration), Nucl. Phys. **A757**, 184 (2005).
[2] J. Adams *et al.* (STAR Collaboration), Nucl. Phys. **A757**, 102 (2005).
[3] B. B. Back *et al.*, Nucl. Phys. **A757**, 28 (2005).
[4] I. Arsene *et al.* (BRAHMS Collaboration), Nucl. Phys. **A757**, 1 (2005).
[5] S. Mrowczynski, Phys. Lett. **B314**, 118 (1993).
[6] P. Arnold, J. Lenaghan, G. D. Moore, and L. G. Yaffe, Phys. Rev. Lett. **94**, 072302 (2005).
[7] A. Rebhan, P. Romatschke, and M. Strickland, Phys. Rev. Lett. **94**, 102303 (2005).
[8] A. Dumitru and Y. Nara, Phys. Lett. **B621**, 89 (2005).
[9] B. Schenke, M. Strickland, C. Greiner, and M. H. Thoma, Phys. Rev. D **73**, 125004 (2006).
[10] S. Scherer, M. Bleicher, S. Haussler, and H. Stocker, Int. J. Mod. Phys. E **17**, 965 (2008).
[11] Z. Xu, L. Cheng, A. El, K. Gallmeister, and C. Greiner, J. Phys. G: Nucl. Part Phys. **36**, 064035 (2009).
[12] K. Adcox *et al.* (PHENIX Collaboration), Phys. Rev. Lett. **88**, 022301 (2002).
[13] C. Adler *et al.* (STAR Collaboration), Phys. Rev. Lett. **89**, 202301 (2002).
[14] S. S. Adler *et al.* (PHENIX Collaboration), Phys. Rev. Lett. **91**, 182301 (2003).
[15] J. Adams *et al.* (STAR Collaboration), Phys. Rev. Lett. **92**, 052302 (2004).
[16] P. Romatschke and U. Romatschke, Phys. Rev. Lett. **99**, 172301 (2007).
[17] K. Dusling and D. Teaney, Phys. Rev. C **77**, 034905 (2008).
[18] H. Song and U. W. Heinz, Phys. Rev. C **77**, 064901 (2008).
[19] S. A. Bass *et al.*, Phys. Rev. C **79**, 024901 (2009), and references therein.
[20] A. Adare *et al.* (PHENIX Collaboration), Phys. Rev. Lett. **101**, 232301 (2008).
[21] S. S. Adler *et al.* (PHENIX Collaboration), Phys. Rev. Lett. **91**, 072303 (2003).
[22] R. Baier, Nucl. Phys. **A715**, 209 (2003).
[23] A. Majumder, J. Phys. G: Nucl. Part. Phys. **34**, S377 (2007); I. Vitev, J. Phys. G: Nucl. Part. Phys. **35**, 104011 (2008).
[24] M. Gyulassy, P. Levai, and I. Vitev, Phys. Lett. **B538**, 282 (2002).
[25] S. S. Adler *et al.* (PHENIX Collaboration), Phys. Rev. Lett. **96**, 032302 (2006).
[26] T. Hirano and Y. Nara, Phys. Rev. C **69**, 034908 (2004).
[27] T. Renk, J. Ruppert, C. Nonaka, and S. A. Bass, Phys. Rev. C **75**, 031902(R) (2007).
[28] A. Majumder, C. Nonaka, and S. A. Bass, Phys. Rev. C **76**, 041902(R) (2007).
[29] E. V. Shuryak, Phys. Rev. C **66**, 027902 (2002).
[30] A. Drees, H. Feng, and J. Jia, Phys. Rev. C **71**, 034909 (2005).
[31] A. Dainese, C. Loizides, and G. Paic, Eur. Phys. J. C **38**, 461 (2005).
[32] B. Cole, Nucl. Phys. **A774**, 225 (2006).
[33] J. Liao and E. Shuryak, Phys. Rev. Lett. **102**, 202302 (2009), and references therein.
[34] S. S. Adler *et al.* (PHENIX Collaboration), Phys. Rev. C **76**, 034904 (2007).
[35] R. J. Fries, B. Muller, C. Nonaka, and S. A. Bass, Phys. Rev. C **68**, 044902 (2003).
[36] S. S. Adler *et al.* (PHENIX Collaboration), Nucl. Instrum. Methods A **499**, 560 (2003).
[37] M. Allen *et al.* (PHENIX Collaboration), Nucl. Instrum. Methods A **499**, 549 (2003).
[38] C. Adler *et al.*, Nucl. Instrum. Methods A **470**, 488 (2001).
[39] L. Aphecetche *et al.* (PHENIX Collaboration), Nucl. Instrum. Methods A **499**, 521 (2003).
[40] S. Afanasiev *et al.* (PHENIX Collaboration), Phys. Rev. Lett. **99**, 052301 (2007).
[41] J.-Y. Ollitrault (1997), nucl-ex/9711003.
[42] T. Sjostrand, S. Mrenna, and P. Skands, J. High Energy Phys. 05 (2006) 026.
[43] A. Adare *et al.* (PHENIX Collaboration), Phys. Rev. C **78**, 014901 (2008).
[44] A. Adare *et al.* (PHENIX Collaboration), Phys. Rev. C **77**, 064907 (2008).
[45] A. Adare *et al.* (PHENIX Collaboration), Phys. Rev. Lett. **98**, 162301 (2007).
[46] J. Adams *et al.* (STAR Collaboration), Phys. Rev. C **72**, 014904 (2005).
[47] B. B. Back *et al.* (PHOBOS Collaboration), Phys. Rev. C **72**, 051901 (2005).
[48] M. L. Miller, K. Reygers, S. J. Sanders, and P. Steinberg, Annu. Rev. Nucl. Part. Sci. **57**, 205 (2007).
[49] V. S. Pantuev, JETP Lett. **85**, 104 (2007).
[50] N. Armesto, C. A. Salgado, and U. A. Wiedemann, Phys. Rev. C **72**, 064910 (2005).
[51] P. Aurenche, F. Gelis, and H. Zaraket, Phys. Rev. D **62**, 096012 (2000).